

Switching based Spin Transfer Torque Oscillator with zero-bias field and large tuning-ratio

Gaurav Gupta^{1,2†}, Zhifeng Zhu² and Gengchiau Liang²

¹Spin Devices, Delhi 110006, India

²Department of Electrical and Computer Engineering, National University of Singapore,
Singapore 117576

We propose a novel concept of obtaining oscillations with frequencies in very-high frequency (VHF) and ultra-high frequency (UHF) bands. A traditional spin torque nano-oscillator (STNO) consists of at least one pinned layer (PL) and one free layer (FL) which precesses in a fixed orbit, defined by a precession angle, which results in magneto-resistance (MR) oscillations. In STNO, with aligned or even orthogonal easy-axis of the magnetic layers and with or without external bias magnetic field, it is not possible to attain full MR swing. The constricted MR swing jeopardizes the extracted output power. Furthermore, the orbit is strongly disturbed by the thermal fluctuations resulting in strong magnetic noise. In stark contrast to the operation principle of a STNO, we theoretically demonstrate, with the practical parameters from the experiments, that with a unidirectional current in a dual asymmetric free-layers (with no pinned layer) based perpendicular magnetic tunnel junction (pMTJ), both of the free layers can attain a complete and out-of-phase self-sustained switching without the aid of any external magnetic field. This design facilitates a switching based spin torque oscillator (SW-STO) with a full MR swing, and hence a larger output power, for stable and more thermally robust free-running oscillations. Furthermore, the integration with the n-type metal-oxide-semiconductor (NMOS) field-effect transistors at 130, 65 and 14 nm node is appraised to expound its effect on the oscillator performance, controllability with DC bias and the design constraints, to demonstrate the viability of the design as a dynamically controllable oscillator for practical on-chip implementation.

I. INTRODUCTION

On-chip oscillators [1] generate stable periodic oscillations, whose voltage (VCO), current (CCO) or digital (DCO) control serves as an integral component of the phase-locked loop (PLL) and radio-frequency (RF) transceivers. PLL generates the clock signal for the chip, where it can either output the same or multiply or divide the VCO frequency to suit the application. Frequency (f) control of the oscillators enables dynamic-frequency-scaling (DFS) scheme [2] for optimizing the low-power modes. Furthermore, as the indispensable blocks in the RF transceiver circuits, oscillators are used for modulation and clock recovery. For these applications, an ideal oscillator requires a large quality factor (Q) (i.e. small phase noise), low power consumption (P_{IN}), large output power or voltage swing (P_O or V_O), integrability with CMOS, large tunability ratio (f_{max}/f_{min}) and small die area occupancy in the desired frequency regime. Extant solutions [1, 3] are based on the ring-oscillators, which have low Q , for sub-GHz and LC-tank oscillators (large Q) for a few GHz range, because the phase noise for the ring oscillators further degrades as the frequency is scaled-up. Furthermore, LC oscillators have small tuning range [1, 4], have large P_{IN} , are difficult to integrate in the very-large scale integration (VLSI) chips and occupy large area because of the large inductor and varactor size even in low GHz regime at which custom-designed chips can operate.

To overcome these issues, recently spin-torque nano-oscillators (STNOs) and spin-hall nano-oscillators (SHNO) have been proposed [5] and integrated with CMOS [6]. They are expected to occupy small area (\sim area of magnetic-tunnel junction (MTJ)), consume less power and provide ultra-wide-band operation [7, 8]. STNOs are based on the precession of a free-layer (or set of locked [9-11] FLs) in MTJ within a certain orbit determined by a precession angle [5], with a single or a set of fixed reference/pinned layer [12]. This precession in a locked orbit results in an oscillatory change in the magnetization of the free layer (s) with respect to that of the reference layer, which translates into a resistance change of a MTJ (or

spin-valve in the case of a metallic spacer), R_{MTJ} and thus an output voltage swing. With the application of a well-controlled and precise bias magnetic field H_{Applied} , large Q for STNO has been obtained [13]. Even in another genre of spin-oscillators based on vortex (VSTO), where an oscillating magnetic vortex is generated in thick magnetic layers of large cross-section via current induced spin-transfer torque (STT) and perpendicular H_{Applied} [14-19] large Q has been observed. However, providing a uniform and precisely stable magnetic field H_{Applied} in the integrated circuits [19] is extremely difficult, which therefore, would make it difficult to control the oscillator characteristics. Hence, there has been a general effort in recent years to research solutions that can operate without H_{Applied} [20-22]. To eliminate the external bias magnetic-field H_{Applied} required in all in-plane or all-perpendicular designs, MTJ stacks with orthogonal set of layers [10, 23] have also been investigated. To increase the output voltage swing by increasing the observable fraction of the MR in the oscillations, the combination of multiple in-plane and perpendicular magnetization free and pinned/reference layers (orthogonal layers) in a MTJ has also been promulgated for a very large precession angle. It enables *near* full rotation of one of the free layers. However, the use of orthogonal layers across the spacer (metal like Cu or insulator like MgO) inherently limits the MR of these stacks. Furthermore, recently, locked precessional orbits of dual free layer designs, i.e. without any polarizing layer, for in-plane magnetization (ii-MTJ) and with assistance of H_{Applied} have also been shown to produce stable oscillatory output [24, 25]. Without H_{Applied} , the output signal has been shown to be very weak (< -100 dBm) [26]. Moreover, for multiple precessional orbits with the resistance oscillations depending on the dynamic angle of the precessions, the effect of the magnetic noise becomes stronger in this design compared to a traditional STNO. Furthermore, sophisticated designs with tilted anisotropy, operating without H_{Applied} , with weak output (< -65 dBm) [21], and more recently with large P_O (nearly -26 dBm at 6.7mA current bias) which need very precise control of H_{Applied} and especially

designed microstructure for the magnet [27, 28] in sombrero-shaped MTJ, have been demonstrated. As a consequence of the reliance on the fixed precessional orbit, the magnetic noise resulting from the thermal fluctuations strongly affects the performance of a STNO (for instance see Fig. 1 of Ref. [29] or Fig. 5 of Ref. [30]), by randomizing the phase of the precession. This especially becomes pernicious when MTJ area is down-scaled because the thermal field scales as an inverse root of the magnet volume. These issues greatly limit its applicability in the real applications [7].

Therefore, in this work we propose a simple design of a spintronic oscillator, with no exotic structure or tilted anisotropy constraints, as conceptually illustrated in Fig. 1. The generated oscillations (50-960 MHz) are in VHF (30-300 MHz) and UHF (300-1000 MHz) frequency bands [31] which more generally serve application-specific integrated circuits (ASICs) [2, 32-36]. Furthermore, this frequency range also serves the RF band for LoRa protocol (868 MHz for Europe, 915 MHz for North America and 430 MHz for Asia) [37-39] deployed for low-cost bi-directional secure low-power wide-area-network (LPWAN) wireless communication channel in internet-of-things (IoT), machine-to-machine (M2M), smart city and industrial applications [40]. This is in contrast to STNO which is normally over this range and gets to tens of GHz and thus applied as microwave source/detector and in wireless transceivers [5, 7] for other protocols like Bluetooth and Wi-Fi. The proposed design is based on dual asymmetric free-layers, with no pinned layer, in a perpendicular magnetic tunnel junction (pMTJ) and operates without any bias magnetic field. The design has a large tunability ratio. The importance of a large tunability ratio is specifically explained in section III.C. The proposed device can also deliver a relatively large output power because MR oscillations attain a full theoretical maximum. This in turn would be much larger than for MTJs with magnetic layers with orthogonal easy-axis. To achieve this, the design deploys a different operation principle than STNO. It is based on the switching of both the free-layers

with a unidirectional current in a pMTJ structure, where one of the free-layer would have traditionally served as a reference layer and mandated current reversal for switching-back the traditional free-layer. The proposed design is subsequently referred as switching based spin torque oscillator (SW-STO). It is shown that both layers can attain complete and out-of-phase self-sustained switching with a DC electrical bias to produce oscillations which are more thermally robust than for a STNO.

The frequency is shown to scale directly with the MTJ current I_{MTJ} . In CCO configuration, the design has tunability of over a decade. This is much superior to STNO [41] and ring oscillators [42] for which even attaining an octave (electronic control for STNO) is a challenge, and thus proposed design is better suited for DFS schemes. CCO would, however, warrant an implementation of the stable current sources/mirrors over a wide operating range. This would heavily penalize the design in terms of power and area. Therefore, simply driving a MTJ with a NMOS in the VCO configuration is also appraised. Therefore, as illustrated in Fig. 2(a), the impact of the integration and the control of the oscillator via foundry calibrated NMOS is also examined across the complementary metal–oxide–semiconductor (CMOS) nodes (130, 65 and 14 nm). Either the gate voltage V_{GS} (suggested method in this work) or the node voltage V_{DD} (akin to the ring oscillator based VCOs) of the cell is tuned, where a cell is referred to a system of a MTJ with a (or set of) driving transistors. It is shown that integrating a transistor has a significant impact on the performance metrics of the oscillator. The performance in general degrades, yet is shown to be better than traditional STNOs in the CCO configuration. Furthermore, we show that the NMOS area dominates the cell-size instead of the MTJ area, and hence, should be the one compared with the traditional ring or LC oscillators to claim the area benefits. Moreover, a larger node because of its larger supply voltage has better current drive and thus an iso-frequency comparison exhibits a smaller channel area and a larger output power for a larger node.

The article is organized as follows. In Sec. II, the methodology of our theoretical simulation of the proposed design is explained. Sec. III discusses the results and is anatomized into four sub-sections. In sub-section III.A, the operation principle and the device physics is expounded, the effect of thermal fluctuation i.e. magnetic noise is considered in III.B. Results for the design driven by a current-source thus operating it in a CCO configuration is presented in III.C, while integration of transistors to operate in a VCO and a DCO configuration is assayed in III.D. This is followed in Sec. IV with the summary and the conclusions of our study.

II. METHODOLOGY

The simulation framework illustrated in [Fig. 2\(b\)](#) expounds all mechanisms considered in this work, and the flow of the variables across the framework. Two methods are considered in this work to drive a unidirectional current through a pMTJ based proposed oscillator. The first one is a constant current source (akin to suggested for a STNO) which operates the device in the CCO configuration ([Fig. 1](#)), and corresponds to only the MTJ dynamics in the framework. The second one is integrating an NMOS with a MTJ on the drain end of the transistor whose supply node V_{DD} (akin to ring-oscillators) or gate (suggested method for this design) is controlled via input DC voltage, which operates the design in the VCO configuration ([Fig. 2\(a\)](#)). This invokes the full framework shown in [Fig. 2\(b\)](#). Other configurations, like a MTJ on the source end or use of the MOS in the diode mode results in an inferior performance of the oscillator and thus not shown here.

The magnetization dynamics is solved via coupled Landau–Lifshitz–Gilbert (LLG) equation integrated via fourth order Runge-Kutta method [[43-45](#)]. An alternate method for solving this stochastic partial differential equation (SPDE) is first-order Euler method [[46, 47](#)], and the trade-offs for both the methods are discussed in Refs. [[44, 48](#)] for a more

interested reader. The dynamics of both the FLs is analyzed via macrospin model which has been shown to be valid in scope of the dimensions considered in this work [49-51]. The problem is numerically solved in Matlab which is dynamically coupled with SMASH to solve at every time-interval Δt of 5 ps for an updated angle between the two magnetization vectors and the voltage across the MTJ. To find suitable Δt , for a few random sets of physical and electronic parameters within the operational regime of the design, frequency of the oscillator was plotted against Δt swept from 250 fs to 12.5 ps. The trend was observed to remain saturated from 250 fs to 8 ps after which it rolls-off because of the error induced in the LLG equation due to a large time step. Within this saturated region, the value of 5 ps was chosen because the run time was exactly divisible by this time-step and thus allowed to exactly count the cycles, and furthermore being a coarse enough value enabled us to reduce the computational time and storage without affecting the results. The oscillator characteristics are extracted for 10 μ s run which results in two million sampling points of the data. It is subsequently parsed by Fast-Fourier Transform (FFT) to extract the oscillator characteristics like fundamental frequency, linewidth, quality factor and output voltage swing V_O . The output power P_O in dBm is computed as $10 + 20 \log_{10}(V_O)$. For input-power P_{IN} and area, in a CCO configuration only MTJ is considered (akin to the STNO literature) while in a VCO configuration both MTJ and transistor are accounted. Next, the Resistance-Area product or $RA = 4.7 \Omega\text{-}\mu\text{m}^2$ is taken from CoFeB pMTJ from imec [52] with zero-bias TMR (Tunneling Magnetoresistance) i.e. $TMR_0 = 143\%$ and MgO thickness $t_{MgO} = 1$ nm. Throughout the text, MTJ dimensions (in nm) along x, y and z axis are respectively expressed as: length \times width \times thickness_{FL₁} (thickness_{FL₂}), with default value of 50nm \times 50nm \times 1.6nm(1.2nm). Both damping and field-like torque (DLT and FLT), $a_{||}$ and a_{\perp} respectively, are considered in the coupled LLG equation as [53],

$$\left(\frac{1+\alpha^2}{\gamma}\right)\frac{d\mathbf{M}_i}{dt} = -\mathbf{M}_i \times [\mathbf{B}_{\text{Eff}}^i - (a_{\perp}^i + \alpha a_{\parallel}^i)\mathbf{p}_j] - \frac{\mathbf{M}_i}{M_s} \times \left\{ \mathbf{M}_i \times [\alpha \mathbf{B}_{\text{Eff}}^i - (\alpha a_{\perp}^i - a_{\parallel}^i)\mathbf{p}_j] \right\} \quad (1)$$

where $\alpha = 0.01$ [53] is the damping constant, γ is the gyromagnetic ratio, $i = 1$ and 2 denotes FL_1 and FL_2 , respectively, and \mathbf{M}_i is the magnetization vector of the i^{th} FL. Corresponding magnetization unit vector \mathbf{m}^i is expressed as $[m_x^i \ m_y^i \ m_z^i]$. \mathbf{p}_j is the unit-vector of the spin-angular momentum acting on the magnetic moments of the i^{th} FL due to the j^{th} FL, where $i \neq j$. Hence, \mathbf{p}_j for the FL_2 dynamics is parallel to \mathbf{M}_1 , while for the FL_1 dynamics it is anti-parallel to \mathbf{M}_2 . $M_s = 1.2573 \times 10^6$ A/m [54] is the saturation magnetization of CoFeB based FL, $\mathbf{B}_{\text{Eff}}^i$ is the effective magnetic field acting on the i^{th} layer obtained as (superscript i is implied, wherever applicable, in all equations below),

$$\mathbf{B}_{\text{Eff}} = \mathbf{B}_{\text{Applied}} + \mathbf{B}_{\mathbf{K}} + \mathbf{B}_{\text{Dipole}} - \mathbf{B}_{\text{Demag}} + \mathbf{B}_{\mathbf{T}} \quad (2)$$

where $\mathbf{B}_{\text{Applied}}$ is a external bias magnetic field and set to zero vector in this work, $\mathbf{B}_{\mathbf{K}}$ is a uniaxial crystalline anisotropy field obtained as,

$$\mathbf{B}_{\mathbf{K}} = \frac{2}{M_s} \left(K_{\text{Bulk}} + \frac{K_{\text{Interface}}}{t_{\text{FL}}} \right) [0 \ 0 \ m_z]^T \quad (3)$$

where $K_{\text{Bulk}} = 2.245 \times 10^5$ J-m⁻³ and $K_{\text{Interface}} = 1.286 \times 10^{-3}$ J-m⁻² [54] are the bulk and interface anisotropy constant respectively, t_{FL} is the free-layer thickness in meter, $\mathbf{B}_{\text{Dipole}}$ is the dipolar field acting on the i^{th} layer due to the presence of the j^{th} layer and expressed as,

$$\mathbf{B}_{\text{Dipole}}^i = \mu_0 M_s \begin{bmatrix} D_{xx} & D_{xy} & D_{xz} \\ D_{yx} & D_{yy} & D_{yz} \\ D_{zx} & D_{zy} & D_{zz} \end{bmatrix} \begin{bmatrix} m_x^j \\ m_y^j \\ m_z^j \end{bmatrix} \quad (4)$$

where \mathbf{D} is the 3×3 dipolar-tensor and is calculated directly via analytical expressions from Ref. [55, 56]. $\mathbf{B}_{\text{Demag}}$ is the self-demagnetizing field of the FL, whose vector is expressed as,

$$\mathbf{B}_{\text{Demag}} = \mu_0 M_s [N_x m_x \ N_y m_y \ N_z m_z]^T \quad (5)$$

where N_x , N_y and N_z is computed via expressions in Ref. [57]. The thermal fluctuation field which induces magnetic noise in both the FLs is computed as [50, 58],

$$\mathbf{B}_T = \sqrt{\frac{2\alpha K_B T}{(1+\alpha^2)\gamma M_S \text{Vol}_{\text{FL}} \Delta t}} \begin{bmatrix} R_{0,1}^x & R_{0,1}^y & R_{0,1}^z \end{bmatrix}^T \quad (6)$$

where K_B is the Boltzmann constant, Vol_{FL} is the volume of the FL. Along x, y and z-axis, independent random numbers $R_{0,1}$ have Gaussian distribution of zero mean and unit standard deviation. The thermal fluctuation field is accounted at every time-step. Here, we note that the current induced self-heating effects [59-61] have not been included in this work. For high quality MgO MTJs, which lack metallic pinholes in the tunnel junction either due to the fabrication process or a small cross-section of the MTJ [62], it was experimentally proven [63, 64] that joule heating is not the underlying mechanism for the dielectric breakdown. Instead it is the strong electric field larger than 2 V/nm across MgO insulator [63] that results in the dielectric breakdown. Since, in this work, we ensure that the electric field is always weaker than 1 V/nm and also picked parameters from a high-quality pMTJ [52], these secondary effects are ignored in our analysis. Nevertheless, in case the joule heating dominates or is substantial enough to affect the oscillator characteristics, the characteristics should in general degrade because of the increase in the magnetic noise and the slight degradation in the spin-polarization of the carriers [65]. Next, the MTJ resistance R_{MTJ} calculation accounts for the voltage dependence of the TMR and the dynamic angle θ between the two precessing FLs as,

$$R_{\text{MTJ}} = R_P + \frac{R_{\text{AP0}} - R_P}{1 + \frac{V_{\text{MTJ}}^2}{V_{\text{Half}}^2}} \left(\frac{1 - \cos(\theta)}{2} \right) \quad (7)$$

where $V_{\text{Half}} = 0.4$ V, extracted for CoFeB from Ref. [66], is the voltage across the MTJ at which the TMR becomes half of its value at the zero-bias i.e. $\text{TMR}_0/2$. R_P is the MTJ resistance when both the magnets are exactly parallel to each other and remains invariant to

V_{MTJ} for all practical purpose [67, 68], while R_{AP0} is the MTJ resistance when both the magnets are exactly anti-parallel to each other at the zero-bias. For both FLs, an equal spin polarization P is assumed and computed from the Julliere formula for TMR [69] as $\text{TMR}_0 = 2P^2/(1-P^2)$. The STT efficiency $\eta_{i>j}$ for spin-flux from the layer ‘i’ to ‘j’ is computed via Slonczewski expression for MTJ with both sandwiching ferromagnets (FMs) of equal polarization [70],

$$\eta_{1>2} = -\eta_{2>1} = \frac{P/2}{1 + P^2 \cos(\theta)} \quad (8)$$

The expression for η with multiple reflections of the spin-flux has been developed for spin-valves [71-73], as noted in Ref. [74] it may not be applicable on MTJs. Next, the DLT with linear dependence on the V_{MTJ} and FLT with the quadratic dependence on the V_{MTJ} are respectively obtained as,

$$a_{\parallel}^i = \frac{\hbar}{2e} \frac{\eta_{j>i}}{\text{Vol}_{\text{FL}}^i R_{\text{MTJ}}} V_{\text{MTJ}} \quad , \quad a_{\perp}^i = v \frac{\hbar}{2e} \frac{\eta_{j>i}}{\text{Vol}_{\text{FL}}^i R_{\text{MTJ}}} V_{\text{MTJ}}^2 \quad (9)$$

where e is the electronic charge and $v = 2.97/7.82 \text{ V}^{-1}$ is the ratio between the torques extracted from Ref. [67] (for range of values in literature see Table 2.1 and 2.2 of thesis from Kerstin Bernert [75]).

The voltage-dependent MTJ resistance is coded in Verilog-A. The output and transfer characteristics of the high performance NMOS are extracted from the following experimental data from the major foundries presented in IEDM (IEEE International Electron Device Meeting) over the years: 130 nm node bulk-NMOS data from Fig.4 and Fig. 6 of Intel transistors published in Ref. [76], 65 nm node bulk-NMOS data from Fig. 6 and Fig. 7 of IBM, Chartered and Infineon transistors published in Ref. [77], while 14 nm node FinFET (Fin Field Effect Transistor) from Fig. 5 and Fig. 6 of Intel transistors published in Ref. [78]. The channel area for 130 nm and 65 nm is computed as product of channel-length times channel-width, while for 14 nm FinFET its gate length times fin pitch times number of fins

(n), where n is an integer not less than the real number obtained by dividing effective channel-width by fin-width (fin-width = 2 fin-height + fin-thickness). The predictive technology files (PTM) available from University of California Berkley (UCB) have been optimized to fit the transistor characteristics. The transistors are modeled via open-source BSIM4 Verilog-A code from Silvaco for bulk-NMOS and from UCB for FinFETs. The circuit is simulated via SPICE solver SMASH 6.5.0 from Dolphin Solutions. The fitting (red line) of NMOS output characteristics via spice simulation against the extracted data (black circles) is shown for instance in Fig. 2(c) for 130 nm node, Fig. 2(d) for 65 nm node and Fig. 2(e) for 14 nm node. For the VCO configuration, the 65 nm node with $V_{DD} = 1.1$ V, $V_{GS} = 1.1$ V and channel width to length ratio $(W/L) = 21$ for an NMOS, while for the CCO configuration $I_0 = 500$ μ A is chosen as a default configuration unless specified otherwise.

III. RESULTS and DISCUSSION

A. Operation Principle

Figure 1 illustrates the operation principle of the proposed design. For an electron flow along the +z-axis, the transmitted spin-flux oriented parallel to \mathbf{M}_1 acts on FL_2 to attempt to align FL_2 parallel to FL_1 , while the reflected spin-flux from FL_2 which is anti-parallel to \mathbf{M}_2 , attempts to align FL_1 anti-parallel to FL_2 . In addition to the STT effect, the z-component of the dipolar-field between both FLs attempts to align them in parallel, while the x- and y- components of the dipolar field which participate in the dynamics when the FLs are not aligned along the z-axis attempt to align the FLs in the anti-parallel configuration. Moreover, these two sets of contentions, anisotropy field attempts to drive the FLs along the + or -z-axis depending on if \mathbf{M} is above or below the x-y plane, respectively, while the demagnetizing field opposes the magnetization vectors in the respective FLs. For reflected flux to effectuate the switching, FL_1 should be weaker than FL_2 . This implies that the critical

current for switching FL_1 as free-layer in the traditional pMTJ STT device should be less than the value that would have been obtained for FL_2 as a free-layer. This criterion implies that FL_1 should have weaker PMA (perpendicular anisotropy), i.e. it should be thicker, than FL_2 . For a certain range of values for the physical and electronic constraints, the above effects enable complete and self-sustained successive switching of both the FLs despite of a unidirectional current, as illustrated in the 3D dynamics of the FLs in Fig. 3(a). This is in contrast to a traditional STT device where switching FL into an anti-parallel state w.r.t. reference layer necessitates a current reversal. The set of FL_1 and FL_2 periodically move across up-up ($\uparrow\uparrow$), to down-up ($\downarrow\uparrow$), to down-down ($\downarrow\downarrow$) to up-down ($\uparrow\downarrow$) state, where up (\uparrow) and down (\downarrow) refer to magnetization along the $+$ or $-z$ -axis, respectively, which results in a resistance switch between the parallel and the anti-parallel state, as illustrated in Fig. 3(b). When FLs are in an up-up state, the up-spins act on FL_2 but the down-spins act on FL_1 . In this case, the FL_2 is receiving spins of the same orientation as its magnetization and hence, FL_2 remains unaffected. However, for FL_1 , if the current is above the critical current required to switch FL_1 into an anti-parallel state, after a certain incubation delay, FL_1 would start to flip to drive pMTJ towards a down-up state. In this state, FL_1 receives the spin-flux oriented along the same direction as \mathbf{M}_1 and hence is unaffected. Nevertheless, this transition dynamically starts to change the spin-vector received by FL_2 which now tries to follow switching of FL_1 to align in parallel with it and attempts to drive the pMTJ into a down-down state. At the same time, the reflected spin-vector also changes because of the instantaneous change in \mathbf{M}_2 and attempts to push FL_1 to again drive pMTJ into an up-down state. These competing effects in asymmetrically designed FLs ensure that FLs flip each other in stable self-sustained oscillations. We would like to emphasize that this explanation is somewhat oversimplified to enable conceptual understanding of the operation. As can be gauged from the dynamics in Fig. 3(a), the transient magnetization states would rarely be in a clear set of

up and down states. Mostly they would have a significant x and y component, thus empowering the contentious effects of the dipolar-coupling to play a significant role in the dynamics. Therefore, as evident in Fig. 3(b), one FL may start to switch before another FL is fully switched. The FL dynamics is, on the other hand, such that although \mathbf{M}_1 and \mathbf{M}_2 mostly do not simultaneously exactly align with the z-axis, they do achieve exact parallel and anti-parallel states. This enables the design to achieve a full resistance swing from R_P to R_{AP} and vice-versa. This design attains theoretical maximum swing, with a constant current input, that can be obtained via STT oscillation, which to the best of our knowledge is not possible even in the STNOs with the in-plane FL with a perpendicular polarizer (pi-Fixed) and the perpendicular FL with an in-plane reference layer (ip-Fixed) [20, 41, 79, 80], indicating a novel concept of obtaining oscillations.

These oscillations in resistance electronically translate to the voltage oscillations across a MTJ as shown in Fig. 3(c). The change in R_{AP} and R_{MTJ} as the voltage across the MTJ changes is taken into account as discussed in the methodology section via eq. (7). FFT of the output V_{MTJ} is shown in Fig. 3(d) and 3(e) in dBm (to show output power) and mV units respectively. Figure 3(d) also shows the first two overtones at the multiples of fundamental tone f_0 . The frequency at which the largest output voltage V_{pk} , i.e. the largest output power, is obtained corresponds to f_0 . A 3 dBm line below the peak value (dashed black line) subsequently gives the half-power frequencies f_1 and f_2 on the either side of f_0 . The FFT plot in mV units is manually fitted with the Lorentzian function [25, 81] $V_{pk}/(1+((f-f_0)/\Gamma)^2)$ (blue line in Fig. 3(e)), where Γ is a fitting parameter. The intercept of the function with the -3 dBm line gives f_1 and f_2 , linewidth f_2-f_1 , and quality-factor (Q) which equals $f_0/(f_1-f_2)$. In Fig. 3(c), an abnormal observation in this design is the strong amplitude-fluctuations for small V_{MTJ} i.e. when the FLs are or nearly parallel to each other. These fluctuations occur because of the strong dipolar coupling between the FLs which tends to lock them together.

This assisted with a net FLT makes one FL precess around another while DLT tries to align them via damping effect, governed by the damping factor α . Increasing the α , weakening the dipolar field or weakening the FLT reduces this noise, but the frequency of the oscillator also reduces. Furthermore, for a very high frequency at the large currents, i.e. for very fast switching, the overlap between the dynamics of FL_1 and FL_2 is such that the transient angle between the FLs do not reach full 0 and 180 degree, rather the window starts to diminish which degrades the device performance as shown later. Hence, further research into reducing these amplitude-fluctuations (noise), without compromising with the frequency, would significantly increase the output power P_O of the SW-STO and thus would be an important future direction.

B. Magnetic Noise

Next, we investigate the effect of the thermal fluctuation field that induces a random phase to the magnetization dynamics [82] of both the FLs. Thermal fluctuation field results in a Gaussian noise and modeled by eq. (6). It strongly depends on the volume of the magnet Vol_{FL} . Figure 4(a) shows that despite of magnetic noise both the FLs of the SW-STO still switch and oscillate between $m_z = -1$ and $+1$. Figure 4(d), 4(e) and 4(f) respectively illustrate the 3D magnetization dynamics and FFT of the V_{MTJ} in dBm and mV for an ip-MTJ based STNO of $60nm \times 40nm \times 5nm(1.8nm)$ dimensions, with a fixed in-plane pinned layer in place of the FL_1 in absence of magnetic noise, while the same is respectively illustrated in Fig. 4(g), 4(h) and 4(i) with magnetic noise. This device can also be operated without any external bias field and generate oscillations in the microwave range. Figure 4 illustrates that although a magnetic noise adversely affects the oscillator performance, the SW-STO is much more immune to the thermal field than the precessional orbit-based STNO. To show this, the effect of magnetic noise is compared on SW-STO and a precessional orbit-based STNO (see

trajectory in Fig. 4(d, g)) made of MTJ with same RA-product, FL of similar volume and delivering same output power (-22.5 dBm or 23.7 mV, compare peak of Fig. 3(d) with 4(e) or 3(e) with 4(f)) in the absence of magnetic noise. For SW-STO, the peak output power P_O drops by -10.64 dBm in Fig. 4(b) w.r.t. peak P_O in Fig. 3(d) without the thermal field. The V_{Pk} goes down to 6.8 mV and linewidth increases from 1.67 MHz to 28.16 MHz i.e. Q degrades from 204 to 12.43 . This degradation in oscillator characteristics, however, is quite modest to what is observed for the precessional orbit based STNOs. Magnetic noise strongly impairs the orbit as shown in Fig. 4(g) which degrades the peak P_O by -25.38 dBm (compare peaks in Fig. 4(e) with 4(h)), the peak voltage V_{Pk} goes down to 1.3 mV and the linewidth increases from 0.0874 MHz to 335.7 MHz i.e. Q degrades from 58760 to 15.33 for the STNO. The power gets distributed into the adjacent frequencies which broadens the linewidth and degrades the Q factor. Also compare the output power and the voltage in the presence of the magnetic noise between SW-STO and STNO in Fig. 4(b, c) with Fig. 4(h, i) respectively to observe the relative robustness of SW-STO w.r.t. traditional precessional orbit based STNO. It is found that the SW-STO achieves relatively more thermal stability because of the complete switching into the highly stable states ($z = \pm 1$) along the z -axis where both of the layers spend some time (see flat portion of the waveforms in Fig. 3(b) and 4(a)) before continuing with their transience to toggle again. During these rest periods the anisotropy fields are strong, while the in-plane demagnetizing field that would have pushed away the alignment of the magnetization from the z -axis is nearly zero. For a brief period when the two FLs are in a fully switched AP-state, even the spin-torque due to the current is practically zero. In contrast to STNOs, the attainment of the stable state also allows the device to attain a stable resistance value for the MTJ for a certain duration and that too when the thermal fluctuation would have weakest effect on the dynamics of the oscillator. For STNOs, since the magnetic noise impairs the orbit of the magnetization vectors, it results in a stronger

degeneration of the precise dynamic angle between the FLs thereby affecting the resistance and subsequently the V_{MTJ} oscillations. Since, magnetic noise affects both the amplitude-noise and the phase-noise (quality factor) of the spintronic oscillators, the transient characteristics of a STNO become more chaotic than for a SW-STO.

Since, in this work, switching based design is investigated for only a free-running case, for a rightful evaluation, we compare only with a free-running STNO. Injection locking or synchronization of the magnetization dynamics in the STNOs [24, 25] and the phase-locking in the ring-oscillators [42] dramatically improves their Q, and may have similar benign effect on the proposed SW-STO. Furthermore, since when FLs are nearly locked parallel with each other and one FL starts to precess around the other FL resulting in the rapid oscillations (c.f. Fig. 3(b)), some technique to suppress or rapidly damp these oscillations should greatly enhance the quality-factor of the SW-STO. Investigating these techniques, however, is beyond the scope of the current work and could be a possible future direction to further the investigation of this design. Therefore, for the precessional orbit-based designs (free-running case) scaling down the MTJ dimensions has much worse and stronger effect than on a switching based design which thus withstands better chances of down-scaling of the magnets.

As noted earlier in operation mechanism, there is a physical constraint in pairing of the thickness of the FLs which determines the operability of the design. As a result, Fig. 5 appraises the effect of the FL thickness on the device operation to show that the design can be optimized to meet the frequency requirements over a range of specifications. To reiterate, for a device to work as per our chosen current direction, FL_1 should be weaker (in this case thicker and hence closer to the critical thickness at which magnet would become in-plane) than FL_2 , so that FL_1 can switch from the reflected spin-flux. As observed from Fig. 5, a smaller difference in the thickness of the two FLs increases the frequency. This, however,

reduces the stability of the oscillations such that they die out as the two thicknesses approach each other. As a result, for a smaller difference in the thickness, although frequency increases, the current controlled tunable range degrades.

C. CCO Configuration

Figure 6 presents the oscillator characteristics for operation in a CCO configuration. To focus only on the MTJ dynamics, we do not account for the power, area and the design of the current sources/mirrors which would drive these oscillators, in sync with the STNO literature where it is dealt separately [8, 83]. Integration with the driving transistor(s) will be addressed in the next sub-section. In Fig. 6(a), a wide tuning range from 71 MHz at 195 μ A to 965 MHz at 1100 μ A (red stars) i.e. a tuning ratio of 13.6 is presented. More detailed comparison of the entire performance metrics is given in Table I. It can be found that it is much larger than the values reported for STNOs for current control [20, 41, 79, 80] and the ring-oscillators [42]. The output V_{MTJ} (blue circles) roll-down from -26.24 dBm at 172.5 MHz to -47.7 dBm at 965 MHz. As the current increases, the voltage drop across MTJ also increases. This reduces R_{AP} , the maximum resistance of the MTJ for a given operating bias for the anti-parallel state. As a result, the maximum attainable swing for the resistance oscillations decreases as the voltage drop across the MTJ increases. Therefore, despite of the increase in the current, the V_{MTJ} swing decreases. On the other hand, if there had been no such dependence of the TMR on the voltage bias, the V_{MTJ} swing would have increased. In fact this is indeed observed for small enough currents in Fig. 6(a) (blue stars) where increase in the current over powers the reduction in R_{AP} to result in an increasing trend for the P_{O} initially. The effectiveness of the proposed design, nevertheless, becomes more evident on computing the power consumed (red stars) and the power efficiency (blue circles), illustrated in Fig. 6(b). With an increasing current, as would be expected, the P_{IN} increases and the

efficiency decreases. Efficiency of 0.12%, i.e. nearly -3 on the logarithmic scale, for STNO [41] corresponds to -42 dBm of output, while for the proposed design, at this efficiency, the output is -33.5 dBm.

Next, Fig. 6(c) demonstrates that due to the increased noise and the amplitude fluctuations at the large currents, and hence at the higher frequencies, the linewidth (red stars) increases, thereby degrading the Q (blue circles). The linewidth is however also observed to increase at very small frequencies and resulting in small Q. The trend shows weak minima for the linewidth trend and strong maxima for Q-factor in lower half frequency regime, i.e. the best performance is observed in this region and degrades as the current is either reduced or increased. These trends can be understood as follows. As mentioned above in the operation mechanism, at the larger frequencies at the larger currents corresponding to the larger control voltages, the dynamic angle θ between FLs may not reach full 0 and 180 degree and starts to diminish. Alternatively, it can be understood as an increase in the overlap between the transient characteristic of the m_z of the two FLs or the asymmetric phase shift in the transients. In other words, the larger currents trigger faster switching of the two FLs which are affected asymmetrically because of their asymmetric design (different thickness for the same ferromagnetic parameters). This not only slightly reduces the V_O but also increases the importance of the traditional precessional trajectories, and concurrently increases the fraction of the time per cycle spent by one FL to precess around another when they are nearly parallel. The increased weightage or the importance of the precession thus increases the importance or the influence of the magnetic noise on the oscillations, which results in the increased linewidth and the reduced quality factor. On the other hand, as the current decreases, the MTJ current reduces and eventually approaches the value of the critical current required for the switching of each FL. This has following two key implications. First, as expected, the incubation time for the onset of the oscillations, i.e. triggering the oscillator, increases (not

shown) due to weak current. The onset time becomes strongly stochastic due to the magnetic noise which eventually triggers the oscillator. This would have important implications on the write time of a STT memory, but is not a concern for a tunable oscillator because this falls within the wakeup or startup time of the circuit or a chip. The edges of the clock serve as a reference point for measuring time and thus anything before the clock has stabilized becomes immaterial. Second, the incubation-delay from period-to-period in the oscillations becomes more evident, and in fact determines the lower bound of the obtainable frequency. Period-to-period variations happen because the switching is now slow enough to have the FLs in the perfect parallel and anti-parallel states with both \mathbf{M}_1 and \mathbf{M}_2 aligned along the z-axis long enough, rendering the torques to a near zero such that the following effects play a significant role. The role of the dipolar-field becomes important to unlock from these conditions, especially when the FLs are in an anti-parallel configuration. However, more importantly, the dependence on the random thermal-field (magnetic noise) increases to unlock the FLs from these alignments. This becomes the key cause of the period-to-period variations from the oscillations between the R_P and the R_{AP} states, since the random thermal-fields introduce random angle-offsets in θ making one switching cycle faster than the other. Therefore, the linewidth increases and the quality factor decreases for very weak currents. The difference in strength of inflection on the trend for linewidth and quality factor (Q) emerges because later also depends on f_0 . This f_0 which comes in the numerator of the expression for computing Q is small for a small driving current. Hence, the small change in the denominator i.e. linewidth is more strongly reflected in Q . This results in strong maxima for Q for weak minima in linewidth in lower half of the operational window of the oscillator. The points of inflection, however, do not align due to dependence of Q on f_0 . Nevertheless, the observed Q is in the range of 4.2 to 21, which is comparable to the Q -factor for the free-running STNOs [41]. This again affirms the usefulness of the proposed design.

Next, since we have specifically emphasized on the large tunability ratio of the proposed device and here in the CCO configuration shown a ratio of 13.6 which is much larger than other solutions (see Table I for comparison), we explain here the importance of this performance metric. An important issue with the extant solutions is their small tunability ratio, for both semiconductor and spin-based solutions [41, 42, 84]. For the multi-band operation, directly driven by the tunable oscillator (CCO/VCO/DCO), the advantage of a large tunability ratio is implicit. However, in many applications tunable oscillator is integrated within the PLL which then generates the oscillations of the desired frequency, like for clocks in VLSI chips and local oscillator signal for transceivers. Here, despite of a small tunability ratio, even as large as only an octave, of the oscillator it can be propounded that a frequency down-counter of the larger values can be used to achieve even smaller frequencies and thus artificially expand the tunability range with an insignificant increase in the area and cost. It thus appears that there is no need of a large tunability ratio in an integrated tunable oscillator. However, actually there is indeed a need of a large tunability ratio, but not implicit in these systems. It can be understood in detail as follows. In PLL, a divider (frequency down-counter) is implemented in the feedback loop. This divider scales down the frequency by a natural number N programmed into the divider. The output of this divider is thus used as an input to the phase-detector whose other input would be coming from a stable crystal oscillator of generally much lower frequency. Designing a larger N -value divider does not incur much additional area or cost penalty as well. Similarly, even at the output of PLL another frequency down-counter (divide by M -value) can be used, with insignificant increase in the cost and area, which finally gives the desired clock frequency. Hence, an octave band oscillator seems to suffice, provided it can generate large enough frequency that can be down-scaled. This oscillator output can be thus be divided by N and M respectively to generate input for phase-detector and the clock output. Using a large frequency output of the

oscillator (for instance with an octave tunability) just requires a larger value of N and M , which insignificantly increases the cost and area. Unfortunately, not only for the proposed SW-STO (as we show later in results section) but even in general the power consumed by the oscillator increases significantly at the large frequencies. For instance, for a ring-oscillator the dynamic power is directly proportional to the frequency, and the quality-factor degrades (or phase noise increases) tremendously at larger frequencies. Hence, designing a tunable oscillator at much higher frequency than the desired clock frequency strongly penalizes the performance with respect to (w.r.t.) to both the power and the phase noise, and thus the design of the PLL would suffer. Hence, operating the oscillator as close as possible to the clock frequency is a standard design technique. Hence, even for PLL driven multi-band operation, a large tunability ratio is a very much desired characteristic of a tunable oscillator. A decade-wide tunable oscillator can therefore operate with a smaller value of N and M by generating frequency closer to the desired clock output over a wider frequency spectrum and can thus significantly reduce the power consumed in the PLL.

D. VCO Configuration

D.1 Driven by NMOS

From the practical point of view, for the CCO configuration, the MTJ needs to be driven by a tunable constant current source. Designing a current source in turn would need a few transistors. MTJ is fabricated among higher metal layers as part of BEOL (back-end of line) process while these driving transistors are fabricated during FEOL (front-end of line) process. Therefore, topologically, the transistors are laid out under the MTJ. Hence, the larger of the two areas (MTJ or the driving circuit) gives the actual area occupied by the cell. This indicates that only comparing the MTJ area with that of the ring-oscillator to proclaim area advantage for former is not correct. This is an important design consideration often

overlooked in a spin-oscillator literature. Furthermore, it becomes more difficult to design stable widely tunable current sources/mirrors, especially at smaller CMOS nodes [8, 83], than designing VCO/CCO with the wide tuning range. Therefore, we consider the case of driving a MTJ with a single gate-controlled NMOS in this section. Figure 7 illustrates the effect of the transition from a CCO to a gate-controlled VCO configuration. The supply voltage V_{DD} and the gate voltage are fixed whereas the node connecting MTJ with the drain end of the NMOS is floating. The voltage at this node is now the output voltage V_O that would be routed to the subsequent stages driven by the oscillator. Consequently, in a VCO configuration, we compute P_O corresponding to the V_O instead of the V_{MTJ} . It is understood that the oscillatory or the AC component of V_O is just inverted w.r.t. AC component of the V_{MTJ} , and they are different only w.r.t. a DC operating point. As a result, to have a proper comparison of the voltage oscillations between a VCO and a CCO configuration, V_O in Fig. 7, for a constant current source, is inverted by subtracting V_{MTJ} from 1.1 V which is the V_{DD} used for the VCO configuration. Figure 7(a, b) show the R_{MTJ} and V_O for the CCO configuration for comparison with the VCO configuration operating at 350 MHz. To attain this, the CCO configuration is operated at the current equal to the average current observed for the VCO configuration which is 450 μA in this case. As the resistance of the MTJ oscillates, it changes the quiescent or the DC operating point of the drain end of the NMOS. Therefore, it can be found that not only the voltage across the MTJ oscillates but the current through the cell also oscillates, as shown in Fig. 7(c), in anti-phase with R_{MTJ} (Fig. 7(d)) i.e. characteristics of the I_{MTJ} and R_{MTJ} are inverted w.r.t. each other; however, V_O (Fig. 7(e)) oscillates in-phase with the R_{MTJ} . The anti-phase oscillations diminish the output voltage swing. Peak-to-peak voltage swing ΔV can be approximately given by,

$$|\Delta V| \sim |I_{AVG} \cdot \Delta R - R_{AVG} \cdot \Delta I| \quad (10)$$

where I_{AVG} is the average of the oscillating current I_{MTJ} through the cell, R_{AVG} is the average resistance of the oscillating R_{MTJ} , and ΔI and ΔR are the respective peak-to-peak swings in the current and the resistance oscillations. Equation (10) is mathematically implicit from taking partial derivative of $V_{DS} = V_{DD} - I_{MTJ} \cdot R_{MTJ}$ with proper phase for all three variables. It can be observed that ΔV is not equal to twice of V_O . The magnitude of ΔV includes the amplitude-noise while V_O is the amplitude of the swing over the noise floor. Therefore, V_O cannot be extracted manually from the noisy data, and FFT is performed on the obtained data to estimate the V_O . Since, V_O is the actual usable signal, after subtracting for the effect of the noise, corresponding usable peak-to-peak value i.e. $2 \cdot V_O$ is smaller than ΔV . Since ΔV can be calculated even manually from simple arithmetic operation on the transient plots of I_{MTJ} and R_{MTJ} , and thus more intuitive, it serves as a simple tool to conceptually understand the VCO characteristics, presented in subsequent sub-sections. Equation (10) directly implies that the magnitude of the ΔV (which includes noise) for the proposed oscillator, on being driven in a VCO configuration decreases w.r.t. a CCO configuration because ΔI is zero for the later. Consequently, V_O extracted from the noisy data also reduces for the VCO configuration, thereby degrading the output power P_O . Although explicit analysis has not been done for traditional STNO driven by a NMOS like for the proposed design, given the same concept applicable at the drain node for STNO in series with NMOS, we expect similar drop in P_O for the STNO case as well in the same configuration.

Another conceptual approach that should assist in understanding the results in subsequent sub-sections is the load-line analysis (Fig. 8). Load-line analysis is a standard approach [85] to graphically obtain the DC bias or the quiescent point of the system shown in Fig. 2(a), i.e. it gives the DC current through the NMOS and the DC voltage at the drain terminal. In Fig. 8, for simplicity, R_{MTJ} is treated as a constant i.e. a trivial resistor. As shown in Fig. 8(a), for the gate-control or V_{GS} sweep with a fixed V_{DD} , the output characteristics of

the NMOS (solid line) i.e. current I_{DS} vs. drain-to-source voltage V_{DS} characteristic for an increasing gate-to-source voltage V_{GS} is intersected with a single dashed line of the output characteristic of a resistor which intercepts the y-axis at V_{DD}/R_{MTJ} and x-axis at V_{DD} , giving a slope of $-1/R_{MTJ}$. The intersections of these two output characteristics are marked via red dots and give the quiescent point or the operating DC conditions. It can be found that as the V_{GS} increases, the DC voltage at the drain terminal reduce while the MTJ or the drain current increases. In contrast, for the V_{DD} sweep with a fixed gate voltage, shown in Fig. 8(b), load-line analysis shows a single line (actually superimposed, with larger V_{DD} line overshadowing the smaller V_{DD} trend line) for the NMOS output characteristic, and multiple parallel lines for R_{MTJ} of $-1/R_{MTJ}$ slope, one each for an increasing supply voltage V_{DD} . This results in the increase of both the DC voltage at the drain terminal and the drain current when the V_{DD} increases. These concepts would be used in section D.2. Next, when both V_{DD} and V_{GS} are fixed in Fig. 8(c) but the resistance of the MTJ is swept, a single line for the NMOS output characteristic is intersected via respective R_{MTJ} output characteristic line with a corresponding slope. This results in the decrease of both the DC voltage at the drain terminal and the drain current when R_{MTJ} increases. This concept would be useful in understanding section D.3.

D.2. V_{GS} and V_{DD} Control

Figure 9-11 show the control of the oscillator via tuning the gate-voltage V_{GS} and the node voltage V_{DD} . Although both methods show nearly a same frequency tuning range in Fig. 9 and same range of linewidth and quality factor in Fig. 11, of the two methods, superior characteristics like a larger V_O (Fig. 9) and better power efficiency P_O/P_{IN} (Fig. 10) are exhibited for the V_{GS} control of the NMOS. Henceforth, the detailed mechanism behind the observations, their impact on the oscillator performance and the trade-offs for controlling via V_{GS} or V_{DD} are expounded in this sub-section.

Impact on Frequency: For both the gate and the V_{DD} control, the current increases with the voltage which subsequently increases the oscillation frequency (see red stars in Fig. 9). However, it is also observed that the frequency linearly increases on tuning the V_{DD} , while it saturates for a large V_{GS} . This can be understood with the load-line analysis described earlier. In Fig. 8(a), for the gate-control, the quiescent point is in the triode region. As V_{GS} increases, the operational V_{DS} decreases and the I_{DS} increases and both eventually saturate. Conversely, in Fig. 8(b), for the V_{DD} control, if the quiescent point (red dots) enter the saturation region of the transistor, the current has almost no change (slightly increase due to the non-saturating behavior at smaller nodes due to the short-channel effects), but V_{DS} would continue to increase. If a quiescent point is in the triode region, both I_{DS} and V_{DS} would increase continuously. Due to the large R_{MTJ} and a relatively large current requirement to switch the FLs, the voltage drop across the MTJ forces the transistor to operate in the triode region in this work. Following this operating or the DC bias of the system with the NMOS in the triode region, and the current I_{DS} and the drain voltage V_{DS} following the explanation above, the frequency (c.f. Fig. 9; red stars) continuously increases for the V_{DD} control while it saturates for the gate-control of the oscillator.

Thereafter, it can be observed that in a VCO configuration the lowest frequency operable is lower than that in a CCO configuration (see Table I for explicit numbers). At the lowest frequency in the VCO configuration, the average drain current I_{AVG} is lower than the value at which the oscillator works in the CCO configuration. The working of oscillator at such low current can be attributed to the current I_{DS} oscillations in the VCO configuration. During the oscillations, the instantaneous current is much larger than the lowest operating current in the CCO configuration for a substantial fraction of the time-period. This current drive is observed to be still sufficient to trigger the oscillator. At the lowest current drive in the I_{MTJ} oscillation, when the MTJ is in the anti-parallel state, the switching dynamics to

transition the MTJ into a parallel state and thus increase the current drive is sustained mainly via dipolar field.

Impact on Output Power: The downside of the current oscillations in the VCO configuration is to degrade the V_O , as discussed earlier and illustrated in Fig. 7. V_O (blue circles in Fig. 9), however, not only degrades but it also exhibits more complex behavior which can be understood via eq. (10). Succinctly, the increasing trend of V_O is observed when the increase in the current outdoes the fall in the MTJ resistance due to latters dependence on the TMR, whereas a decreasing trend of the P_O is observed just like for a CCO configuration when the increase in the current is insufficient to compensate for the decrease in the R_{MTJ} . To obtain the detailed insights, the detailed mechanism is investigated as follows. The current increases as the V_{GS} or the V_{DD} increases, thus I_{AVG} increase in both cases. Because of the increase in I_{AVG} , the dc bias across the MTJ also increases (Fig. 8). The rate at which this dc bias changes and the extent to which it can change is however different for the two type of controls. For the V_{GS} control, an increase in V_{GS} results in a downward shift in the drain bias which automatically translates to a larger MTJ bias because of a fixed V_{DD} which in turn is set at its maximum value permissible for the node. For the V_{DD} control, an increase in the V_{DD} results in an upward shift in the drain bias. However, this change in the drain bias is not as swift as the change in V_{DD} which thus allows the MTJ bias to increase ($V_{DD} = \text{drain dc bias} + \text{MTJ dc bias voltage}$). This difference in the dynamics of the operating voltages of the drain terminal and the MTJ result in very different trends for V_O . The upper bound due to a smaller V_{DD} in the case of a V_{DD} control, despite of an increasing MTJ dc bias, results in a nearly constant V_O with all values within a small window of only 1.5 dBm with a base value of -44dBm . The points seem to be randomly distributed in this narrow range owing to the finer balance among dc bias, MTJ dynamics and TMR roll-off with the MTJ voltage. Averaging over 16 runs for each of the case of V_{DD} control, however, shows a

trend with a weak maximum in the center as shown via dashed line in Fig. 9(b). The subsequent finer discussion on the effect of V_{DD} control on V_O therefore implicitly refers to this average behavior. Next, because of the dependence of TMR on V_{MTJ} , the R_{AP} , ΔR and R_{AVG} reduce as the current increase in both cases. Since the quiescent point of the drain terminal acts as an additional constraint for regulating the potential drop across the MTJ, it results in constraining of ΔR and R_{AVG} . Consequently, for the V_{DD} control, the $\Delta R \cdot I_{AVG}$ firstly increases and then decreases whereas for the gate-control it always decreases and starts to saturate. The non-linear dependence of the current on the respective voltage control and the non-linear relation between the R_{MTJ} and the V_{MTJ} results in firstly an increasing and then decreasing trend for ΔI (current oscillations) for the V_{DD} control, whereas it is mainly an increasing trend for the gate-control. With the consideration of R_{AVG} and ΔI together, for both the V_{DD} and the gate-control, $R_{AVG} \cdot \Delta I$ continuously decreases with an increasing control voltage. Therefore, the operating dc bias, R_{AVG} , ΔI , ΔR and I_{AVG} collude to result in the change in ΔV with same dependence on the V_{GS} and the V_{DD} control as the trends observed for the V_O or P_O in Fig. 9. For the results of the V_O data, it can also be observed that the gate-control enables a larger P_O again because of the full-scale V_{DD} which equals to the node supply voltage, but a lower V_{DD} because the V_{DD} -control for the oscillator inherently limits the V_O and the P_O . Conspicuously, irrespective of the control, one shortcoming of this design, compared to a ring-oscillator (see Table I) used for the ASIC clocks, is still much lower output power, indicating that an additional amplifier driven by a V_O signal may still be needed and consume additional area and energy. The design of this amplifier, however, is beyond the purview of the current work and hence the configurations in Table I for each column are prudently specified to bring out this difference explicitly to notice.

Impact on consumed power and power-efficiency: Next, the power consumed P_{IN} (red stars) in Fig. 10, as expected, follows the same trend as the current or the frequency for

the respective type of voltage controls. A larger P_O for the gate-control, with P_{IN} in the same range as for the V_{DD} -control, evidently results in a larger power-efficiency P_O/P_{IN} (blue circles) for the gate-control. Furthermore, for the gate-control, the cell does not load the preceding driving stage or the circuit which generates the control voltage because of the large (theoretically infinite) input impedance of the gate terminal of the transistor. For the V_{DD} -control, the drain-to-source impedance is much smaller w.r.t. the gate input impedance and thus loads the driving circuit. Therefore, for practical designs, the gate-control of the oscillator is suggested instead of the V_{DD} -control method of the ring-oscillators.

Impact on linewidth and quality-factor: In the VCO configuration, there are three key factors which result in noise and thus affect the linewidth. First is the amplitude-noise generated when R_{MTJ} tends to R_P (c.f., Fig. 3(c)) i.e. when the two FLs become nearly parallel, one FL starts to strongly precess around another, resulting in the rapid oscillations. Second is the addition of the magnetic noise which has Gaussian random distribution. Third, is the fluctuation in the operating bias of the drain terminal which further degrades the oscillator characteristics (Fig. 7). Therefore, in Fig. 11, the linewidth increases because of the increasing noise with the increasing voltage for both V_{DD} and V_{GS} control. For the first data point of V_{DD} control the current and corresponding frequency are small enough to mark heavy dependence on the magnetic noise which thus increases the linewidth. The physics here is same as observed and explained for very small currents in the CCO configuration. Lastly, the Q factor, computed as $f_0/(f_1-f_2)$ i.e. the ratio of the fundamental tone to the linewidth, follows the simultaneous effect on the fundamental frequency and the linewidth for both a CCO and a VCO configurations. Hence, at both ends of the current strength, the linewidth is larger and the quality factor is smaller than its adjacent points. The Q is in the range of 3.7 to 13.3, which is slightly lower than the values obtained in a CCO configuration for the SW-STO and for the free-running STNOs [41]. The VCO frequency is now in the

range of 47.6 MHz to 276.3 MHz, which limits its applicability to the ASIC clocks, with the tunability ratio of 5.8. This ratio is still much greater than both for the STNOs and the ring-oscillators (see [Table I](#)). These results show that even in the VCO configuration with a single NMOS, the proposed design can contest with the effectiveness of the other oscillator designs.

D.3. MTJ Area

[Figure 12](#) next appraises the effect of scaling the MTJ cross-section for fixed drive strength of the NMOS. As the area of the MTJ is scaled, it proportionately scales the R_{MTJ} because of a constant RA-product. In [Fig. 12\(a\)](#), the oscillator frequency goes down with the increasing area because the current density scale-down almost quadratically with the MTJ dimension. Deviation from the quadratic trend happens because of the changes in the DC bias conditions (see red dots in the load-line analysis illustrated in [Fig. 8\(c\)](#)), due to the change in the R_{MTJ} . As observed in [Fig. 8\(c\)](#), as the R_{MTJ} scales-down for the fixed operating condition of the NMOS, the drain current and the DC voltage of the drain terminal increases while the DC bias across the MTJ i.e. approximately the average value of the V_{MTJ} reduces. This increase in the current, however, cannot over-ride the decrease in the current density due to the quadratic effect of the scaling-up of the MTJ dimension. Hence, the frequency (red stars) scales-down but the trend is weaker than the trend that would have been obtained for pure quadratic effect of area scaling. Fixed RA product also results in scaling down of both ΔR and R_{AVG} which is again weaker because of the smaller DC value of the V_{MTJ} caused by the shift in the bias conditions. The shifts in the bias conditions also allow for much more steep increase in I_{AVG} than in ΔI . This is further assisted positively by an increased thermal stability of the MTJ because the magnetic noise is directly proportional to the square-root of the volume of the magnet. Because of these three reasons, the output power P_O (blue circles) increases with the increasing cross-section but at the cost of the frequency. Increase in the

current also results in the increase in P_{IN} (red stars) as shown in Fig. 12(b), but the improvement in P_O still results in a higher power-efficiency (blue circles) for the larger MTJ cross-sections. Furthermore, as expected from the effect of the volume of the magnet on the magnetic noise, the linewidth (red stars) improves i.e. linewidth decreases as the MTJ cross-section increases in Fig. 12(c). The quality factor, $f_0/(f_1-f_2)$, follows the combined trend of frequency and linewidth. Therefore, it shows local maxima in the center and tapers at the two ends, at the lower end because of large linewidth and at upper end due to small operating frequency. For a 50% increase in the dimension from 50 nm to 75 nm or nearly twice the increase in the area of the MTJ, the linewidth improves from 24 to 14 MHz i.e. by 41.7 %, while the Q factor is nearly 12 for both cases. This shows that if for a given frequency the design permits the use of a larger MTJ, it could be extremely advantageous in terms of the output power, power-efficiency and the linewidth. To examine this viability, we next appraise the scaling of the drive strength of the NMOS across three CMOS nodes and understand how they provide the margin for using larger MTJs despite of scaling-down of the CMOS nodes.

D.4. NMOS W/L Scaling

In Fig. 13, the effect of scaling channel width of NMOS to its length, i.e. W/L ratio, for 14 nm (red stars), 65 nm (blue circles) and 130 nm (magenta squares) CMOS node is studied, integrated with a MTJ of dimensions $50\text{nm} \times 50\text{nm} \times 1.6\text{nm}$ (1.2nm) i.e. a cross-sectional area of $0.0025 \mu\text{m}^2$. As expected the average current I_{AVG} for all three nodes increases with the increasing W/L in Fig. 13(a), and almost saturates because of the integration of the NMOS with the MTJ resistor which determines the DC bias of the system. The channel area is computed based on the approach introduced in the methodology section and illustrated for reference in Fig. 13(b). For 14 nm node, the channel-area is from $0.00168 \mu\text{m}^2$ to $0.0468 \mu\text{m}^2$, for 65 nm node it is from $0.009245 \mu\text{m}^2$ to $0.194 \mu\text{m}^2$, and for 130 nm

node from $0.0245 \mu\text{m}^2$ to $0.5145 \mu\text{m}^2$ for W/L ratio from 5 to 105, respectively. From Fig. 13(a, c), it is found that for 14 nm node, I_{AVG} is from 200 μA at 86.32 MHz to 284 μA at 160.7 MHz for W/L from 10 to 105, for 65 nm node it is from 237.4 μA at 119.2 MHz to 507.8 μA at 357.3 MHz for W/L from 7 to 105, and for 130 nm node from 338.1 μA at 202.2 MHz to 630.2 μA at 486.6 MHz for W/L from 5 to 105, respectively. The node supply-voltage V_{DD} is 0.7 V, 1.1 V and 1.3 V, respectively for the three nodes. Hence, it can be observed from the data that MTJ is always smaller than the channel area of the NMOS. Furthermore, the channel-area of the NMOS is smaller than the actual area of the NMOS which includes the area for the drain and the source region. This shows that firstly the design area would be dominated by the transistor instead of the MTJ and thus should serve as the rightful parameter for comparing area with other designs like the ring oscillators. This fact has often being ignored in the STNO literature. The power and the area of the driving unit have been ignored as well while comparing the designs. Secondly, within the periphery of the folded (because of a large W/L) NMOS, a larger MTJ can be used without any additional penalty on the design area. Therefore, this W/L analysis for the NMOS over three CMOS nodes shows the viability of using larger MTJs to boost the performance of the oscillator. These results also show that the MTJ technology does not need to directly scale-down or at least at the same pace with the CMOS technology for the proposed oscillator. Next, the comparison across the nodes in Fig. 13(d) shows that using larger nodes for the oscillator design would be beneficial as the nominal supply voltage of the node also scales down with it thereby reducing the drive capability of the transistors. On the other hand, the data also implies that scaling-down the CMOS node limits the operational range of the oscillator and for a given current (iso-frequency) degrades the output and consumes more channel area, for instance compare approximately between the last point of 14 nm and the second point of 65 nm trends.

D.5. Digital Control: DCO Configuration

From the frequency range shown in Fig. 13(c), a tunability ratio cannot be computed because channel width is not normally electronically tunable in a VCO or a CCO design. This constraint can be circumvented and channel widths can be electronically controlled by re-configuring a VCO into a DCO. Since the W/L analysis shows that a large channel width for the bulk-NMOS or a large numbers of fins for the FinFETs are required to operate this design, it provides the ability to extend the VCO based analog design to a coarse DCO based digital design, as illustrated in Fig. 14(a). For an N-bit digital control from D_0 to D_{N-1} which corresponds to a digital input from 1 to $2^N - 1$, the width or the number of fins can be discretized across multiple transistors in parallel (wire-ORed i.e. all of the drain terminals are tied together) driving a common MTJ. The effective width of the transistor corresponding to a more significant bit 'm' would be twice the width or twice the number of fins of the transistor corresponding to the adjacent less significant bit 'm-1'. In the DCO design, the gate terminal receives full scale voltage as logic 1 and the transistor is turned-off for logic 0 on receiving 0 V input; hence magnitudes of both its V_{GS} and V_{DD} are fixed. This scheme enables an electronic control of the effective channel width or an effective transistor whose channel-width directly corresponds to the digital input. The lowest digital input of 1 obtained by setting only lowest significant bit to logic 1 and others to logic 0 would correspond to the lowest targeted frequency of the oscillator, while the input $2^N - 1$ obtained by setting all of the N-bits to logic 1 state would correspond to the largest targeted frequency, where the ratio of the largest to the lowest frequency would give us the tunability ratio for the DCO.

Figure 14(b) shows one such example of a 3-bit coarse DCO for 65 nm CMOS node operating with both V_{DD} and V_{GS} at 1.1 V, with gate input being controlled digitally as either 0 V (bit 0) or 1.1 V (bit 1). The channel width of three transistors, W_0 , W_1 and W_2 , is respectively designed to be 7 L, 14 L and 28 L, where L is the channel-length. The digital

input vector $[D_2 D_1 D_0]$ results in 7 possible digital controls 001, 010, 011, 100, 110 and 111, not counting 000 as it turns-off all the transistors and switches off the oscillator. These controls correspond to an effective W/L ratio of 7, 14, 21, 28, 35, 42 and 49. This discretizes the frequency trend of Fig. 13(c) (blue circles) into 7 output frequencies from 119 MHz to 334 MHz, with a tuning ratio of 2.8. The DCO output characteristic in Fig. 14(b) is observed to be saturating, which implies non-linearity in the input-to-output mapping of the digital-control-to-frequency over the designed frequency regime, in-line with the behavior of the current shown in Fig. 13(a). For a larger degree of linearity, DCO can also be re-designed with the largest W/L, corresponding to 2^N-1 input, restricted to be around 20, but it would result in a maximum frequency of 271 MHz for the chosen set of NMOS and MTJ parameters.

IV. SUMMARY

We propose a fundamentally new concept of obtaining oscillations with frequencies in VHF and UHF bands. We posit a novel scheme of the spin-torque oscillators which is based on the superior full-switching of the free-layers in contrast to the extant precessional orbit-based schemes. Moreover, it is shown that the free-layers can be reversibly switched without reversing the direction of the current. Oscillator is shown to operate without any external magnetic field and any pinned layer. Absence of the need of a pinning layer may in fact result in a smaller stack height and integration of the oscillator among lower metallic layers in contrast to standard MTJs which are pushed to higher layers because of a thick stack-size. The oscillator can operate in the range of 48 MHz to 965 MHz, with the tuning ratio of 13.6 (CCO) and 5.8 (VCO), output from -26 to -48 dBm. However, presently, the quality-factor (Q) is in the same range as for free-running STNO and thus need a lot of improvement to come on par with much higher Q, in several hundreds to thousands, indulged

by the precisely biased STNO and/or the synchronized/locked oscillators. Furthermore, although the power-efficiency of a SW-STO in this work is better than that of the STNOs for low frequencies, it becomes much worse on approaching 1 GHz and remains much inferior to the ring oscillators throughout the investigated range. Hence, power efficiency is another performance metric, besides the Q factor and the output power, which needs further work to make SW-STO truly a competitive solution for the tunable oscillators. Next, the analysis including the driving NMOS shows that the NMOS dominates the design area and the larger nodes would be better for driving the proposed oscillator. Moreover, because of the dominance of the transistor on the area, the scaling constraints on the MTJ can be relatively relaxed, and the oscillator performance can be further improved compared to results generally presented in this work. VCO configuration can furthermore be extended into a digital design and used as a DCO. [Table I](#) illustrates some of our exemplar results (second and third column) against other oscillators in the literature. It shows that our design may indeed enable a very large tuning ratio, with a modest Q factor and a very small area for a decent output signal and power-efficiency in the frequency range useful for ASIC clocks and long-range low-power IoT communication via LoRa protocol.

Corresponding Author

[†]gauravdce07@gmail.com

ACKNOWLEDGEMENTS

This work at the National University of Singapore was supported by CRP award no. NRF-CRP12-2013-01 and MOE2013-T2-2-125. We gratefully acknowledge the discussions with Xuanyao Fong, the useful review comments on the manuscript from Kien Trinh Quang and Sachin for helping with Fig. 2.

References

- [1] L. Dai and R. Harjani, Design of High-Performance CMOS Voltage-Controlled Oscillators, Springer US, Boston (2003).
- [2] C.C. Chung, W.S. Su and C.K. Lo, A 0.52/1 V Fast Lock-in ADPLL for Supporting Dynamic Voltage and Frequency Scaling, IEEE Transactions on Very Large Scale Integration (VLSI) Systems 24, 408-412 (2016).
- [3] J.V.D. Tang, D. Kasperkovitz and A.H.M.V. Roermund, High-frequency oscillator design for integrated transceivers, Kluwer Academic Publishers, Boston (2003).
- [4] A. Jha, K. Liao, G. Yeap and K.O. Kenneth, Voltage controlled oscillator area reduction in nano-scale CMOS, in 2014 IEEE Radio Frequency Integrated Circuits Symposium (IEEE, 2014), pp.
- [5] T. Chen, R.K. Dumas, A. Eklund, P.K. Muduli, A. Houshang, A.A. Awad, P. Dürrenfeld, B.G. Malm, A. Rusu and J. Åkerman, Spin-Torque and Spin-Hall Nano-Oscillators, Proceedings of the IEEE 104, 1919-1945 (2016).
- [6] T. Chen, A. Eklund, S. Sani, S. Rodriguez, B.G. Malm, J. Åkerman and A. Rusu, Integration of GMR-based spin torque oscillators and CMOS circuitry, Solid-State Electronics 111, 91-99 (2015).
- [7] H.S. Choi, S.Y. Kang, S.J. Cho, I.-Y. Oh, M. Shin, H. Park, C. Jang, B.-C. Min, S.-I. Kim, S.-Y. Park and C.S. Park, Spin nano-oscillator-based wireless communication, Scientific Reports 4, 5486 (2014).
- [8] T. Chen, P. Dürrenfeld, S. Rodriguez, J. Åkerman and A. Rusu, A highly tunable microwave oscillator based on MTJ STO technology, Microwave and Optical Technology Letters 56, 2092-2095 (2014).
- [9] T. Moriyama, G. Finocchio, M. Carpentieri, B. Azzaroni, D.C. Ralph and R.A. Buhrman, Phase locking and frequency doubling in spin-transfer-torque oscillators with two coupled free layers, Physical Review B 86, 060411 (2012).
- [10] X. Zhu and J.G. Zhu, Bias-Field-Free Microwave Oscillator Driven by Perpendicularly Polarized Spin Current, IEEE Transactions on Magnetics 42, 2670-2672 (2006).
- [11] D.E. Nikonov and G.I. Bourianoff, Spin torque oscillator having multiple fixed ferromagnetic layers or multiple free ferromagnetic layers, US 8604886 B2, Intel Corporation (Priority Date Dec 20, 2010)
- [12] H. Ryo, K. Hitoshi, T. Sumito, T. Shingo, Y. Kay, F. Akio, M. Rie, I. Hiroshi and Y. Shinji, Magnetic field angle dependence of out-of-plane precession in spin torque oscillators having an in-plane magnetized free layer and a perpendicularly magnetized reference layer, Applied Physics Express 9, 053006 (2016).
- [13] M. Hiroki, K. Hitoshi, S. Yoshishige, S. Takayuki, N. Kazumasa, N. Yoshinori, T. Koji, F. Akio, M.D. Alina, A. Koji and Y. Shinji, Large Emission Power over 2 μ W with High Q Factor Obtained from Nanocontact Magnetic-Tunnel-Junction-Based Spin Torque Oscillator, Applied Physics Express 6, 113005 (2013).
- [14] A.D. Belanovsky, N. Locatelli, P.N. Skirdkov, F.A. Araujo, J. Grollier, K.A. Zvezdin, V. Cros and A.K. Zvezdin, Phase locking dynamics of dipolarly coupled vortex-based spin transfer oscillators, Physical Review B 85, 100409 (2012).
- [15] V.S. Pribyl, I.N. Krivorotov, G.D. Fuchs, P.M. Braganca, O. Ozatay, J.C. Sankey, D.C. Ralph and R.A. Buhrman, Magnetic vortex oscillator driven by d.c. spin-polarized current, Nat Phys 3, 498-503 (2007).
- [16] T. Sumito, K. Hitoshi, Y. Kay, K. Makoto, T. Shingo, F. Akio, A. Hiroko, I. Hiroshi, G. Eva, L. Romain, G. Julie, C. Vincent and Y. Shinji, High emission power and Q factor in spin torque vortex oscillator consisting of FeB free layer, Applied Physics Express 7, 063009 (2014).
- [17] S. Petit-Watlot, J.-V. Kim, A. Ruotolo, R.M. Otxoa, K. Bouzehouane, J. Grollier, A. Vansteenkiste, B. Van de Wiele, V. Cros and T. Devolder, Commensurability and chaos in magnetic vortex oscillations, Nat Phys 8, 682-687 (2012).
- [18] Q. Mistral, M. van Kampen, G. Hrkac, J.-V. Kim, T. Devolder, P. Crozat, C. Chappert, L. Lagae and T. Schrefl, Current-Driven Vortex Oscillations in Metallic Nanocontacts, Physical Review Letters 100, 257201 (2008).
- [19] M. Kreissig, R. Lebrun, F. Protze, K.J. Merazzo, J. Hem, L. Vila, R. Ferreira, M.C. Cyrille, F. Ellinger, V. Cros, U. Ebels and P. Bortolotti, Vortex spin-torque oscillator stabilized by phase locked loop using integrated circuits, AIP Advances 7, 056653 (2017).
- [20] F. Ciarán, S. Volker, B. Kerstin, L. Jürgen, F. Jürgen, H.R. William, R.P. Matthew, E.R. Stephen and M.D. Alina, Zero-field spin-transfer oscillators combining in-plane and out-of-plane magnetized layers, Applied Physics Express 7, 043001 (2014).
- [21] S. Witold, S. Tomasz, W. Jerzy, R. Günter and D. Sebastiaan van, Zero-Field Spin Torque Oscillator Based on Magnetic Tunnel Junctions with a Tilted CoFeB Free Layer, Applied Physics Express 5, 063005 (2012).
- [22] A. Hiroko, M. Rie, Y. Shinji and I. Hiroshi, Spin-torque-induced oscillation at zero bias field in a magnetoresistive nanopillar with a free layer with first- and second-order uniaxial anisotropy, Applied Physics Express 8, 083005 (2015).
- [23] C.H. Sim, M. Moneck, T. Liew and J.-G. Zhu, Frequency-tunable perpendicular spin torque oscillator, Journal of Applied Physics 111, 07C914 (2012).
- [24] T. Nagasawa, K. Kudo, H. Suto, K. Mizushima and R. Sato, Large-amplitude, narrow-linewidth microwave emission in a dual free-layer MgO spin-torque oscillator, Applied Physics Letters 105, 182406 (2014).

- [25] M. Al-Mahdawi, Y. Toda, Y. Shiokawa and M. Sahashi, Low-nonlinearity spin-torque oscillations driven by ferromagnetic nanocontacts, *Physical Review B* 93, 024408 (2016).
- [26] P.M. Braganca, K. Pi, R. Zakai, J.R. Childress and B.A. Gurney, Zero field high frequency oscillations in dual free layer spin torque oscillators, *Applied Physics Letters* 103, 232407 (2013).
- [27] M. Hiroki, K. Hitoshi, S. Yoshishige, S. Takayuki, N. Kazumasa, N. Yoshinori, T. Koji, F. Akio, A. Hiroko, T. Tomohiro, I. Hiroshi, A. Koji and Y. Shinji, High Q factor over 3000 due to out-of-plane precession in nano-contact spin-torque oscillator based on magnetic tunnel junctions, *Applied Physics Express* 7, 023003 (2014).
- [28] H. Arai, R. Matsumoto, S. Yuasa and H. Imamura, Spin-Torque Induced Oscillation of a Magnetoresistive Nanopillar with a Conically Magnetized Free Layer and an In-Plane Magnetized Reference Layer, *Journal of the Physical Society of Japan* 85, 063802 (2016).
- [29] L. Bianchini, S. Cornelissen, J.-V. Kim, T. Devolder, W. van Roy, L. Lagae and C. Chappert, Direct experimental measurement of phase-amplitude coupling in spin torque oscillators, *Applied Physics Letters* 97, 032502 (2010).
- [30] Z. Zeng, P.K. Amiri, I.N. Krivorotov, H. Zhao, G. Finocchio, J.-P. Wang, J.A. Katine, Y. Huai, J. Langer, K. Galatsis, K.L. Wang and H. Jiang, High-Power Coherent Microwave Emission from Magnetic Tunnel Junction Nano-oscillators with Perpendicular Anisotropy, *ACS Nano* 6, 6115-6121 (2012).
- [31] Nomenclature of the frequency and wavelength bands used in telecommunications, International Telecommunication Union Rec. ITU-R V.431-438 (408/2015) (Retrieved 19 November 2016).
- [32] R. Giordano, A. Aloisio, F. Ameli, V. Bocci, S. Cadeddu, V. Izzo, A. Lai and S. Mastroianni, Performance of a high-frequency synthesizable digitally-controlled oscillator, in 2014 IEEE Nuclear Science Symposium and Medical Imaging Conference (NSS/MIC), pp.
- [33] C. Zhiqing, Z. Qi, W. Ning, Y. Dunshan, L. Guohong, W. Hui and F. Songlin, A low spur CMOS phase-locked loop with wide tuning range for CMOS Image Sensor, in 2013 IEEE 10th International Conference on ASIC (ASICON), pp.
- [34] Y. Li, L. Liu, X. Huang, R. Zhang and R. Li, Design and ASIC Implementation of High-Speed DDC, in 2011 Second International Conference on Digital Manufacturing and Automation (ICDMA), pp.
- [35] Z. Zhang, Y. Zhiyi, C. Xu and Z. Xiaoyang, A low power 1.0 GHz VCO in 65nm-CMOS LP-process, in 2011 IEEE 9th International Conference on ASIC (ASICON), pp.
- [36] X. Deng, J. Yang and J. Wu, Low jitter ADPLL insensitive to power supply noise, in 2010 IEEE International Conference on Industrial Technology (ICIT), pp.
- [37] Semtech, LoRaWAN Specification v1.0, (January 2015).
- [38] J. Pet, rvi, K. Mikhaylov, H. M. inen and J. Iinatti, Evaluation of LoRa LPWAN technology for remote health and wellbeing monitoring, in 2016 10th International Symposium on Medical Information and Communication Technology (ISMICT), pp.
- [39] J. So, D. Kim, H. Kim, H. Lee and S. Park, LoRaCloud: LoRa platform on OpenStack, in 2016 IEEE NetSoft Conference and Workshops (NetSoft), pp.
- [40] J.P. Bardyn, T. Melly, O. Seller and N. Sornin, IoT: The era of LPWAN is starting now, in ESSCIRC Conference 2016: 42nd European Solid-State Circuits Conference, pp.
- [41] Z. Zeng, G. Finocchio, B. Zhang, P.K. Amiri, J.A. Katine, I.N. Krivorotov, Y. Huai, J. Langer, B. Azzerboni, K.L. Wang and H. Jiang, Ultralow-current-density and bias-field-free spin-transfer nano-oscillator, *Scientific Reports* 3, 1426 (2013).
- [42] H. Gao, L. Sun, X. Kuang and L. Lou, A low-phase-noise ring oscillator with coarse and fine tuning in a standard CMOS process, *Journal of Semiconductors* 33, 075004 (2012).
- [43] W. Skowroński, P. Ogrodnik, J. Wrona, T. Stobiecki, R. Świrkowicz, J. Barnaś, G. Reiss and S.v. Dijken, Backhopping effect in magnetic tunnel junctions: Comparison between theory and experiment, *Journal of Applied Physics* 114, 233905 (2013).
- [44] M. Franchin, Multiphysics simulations of magnetic nanostructures, School of Physics and Astronomy, University of Southampton, (2009).
- [45] S. Sharma, B. Muralidharan and A. Tulapurkar, Proposal for a Domain Wall Nano-Oscillator driven by Non-uniform Spin Currents, *Scientific Reports* 5, 14647 (2015).
- [46] W. Scholz, T. Schrefl and J. Fidler, Micromagnetic simulation of thermally activated switching in fine particles, *Journal of Magnetism and Magnetic Materials* 233, 296-304 (2001).
- [47] M.J. Werner and P.D. Drummond, Robust Algorithms for Solving Stochastic Partial Differential Equations, *Journal of Computational Physics* 132, 312-326 (1997).
- [48] D.V. Berkov and N.L. Gorn, Numerical Simulation of Quasistatic and Dynamic Remagnetization Processes with Special Applications to Thin Films and Nanoparticles, *Handbook of Advanced Magnetic Materials*, Springer US, Boston, 794-880 (2006).
- [49] Z. Li and S. Zhang, Magnetization dynamics with a spin-transfer torque, *Physical Review B* 68, 024404 (2003).

- [50] A. Jaiswal, X. Fong and K. Roy, Comprehensive Scaling Analysis of Current Induced Switching in Magnetic Memories Based on In-Plane and Perpendicular Anisotropies, *IEEE Journal on Emerging and Selected Topics in Circuits and Systems* 6, 120-133 (2016).
- [51] Y. Zhou, H. Zhang, Y. Liu and J. Åkerman, Macrospin and micromagnetic studies of tilted polarizer spin-torque nano-oscillators, *Journal of Applied Physics* 112, 063903 (2012).
- [52] G.S. Kar, W. Kim, T. Tahmasebi, J. Swerts, S. Mertens, N. Heylen and T. Min, Co/Ni based p-MTJ stack for sub-20nm high density stand alone and high performance embedded memory application, in 2014 IEEE International Electron Devices Meeting, pp. 19.1.1-19.1.4.
- [53] A.A. Timopheev, R. Sousa, M. Chshiev, L.D. Buda-Prejbeanu and B. Dieny, Respective influence of in-plane and out-of-plane spin-transfer torques in magnetization switching of perpendicular magnetic tunnel junctions, *Physical Review B* 92, 104430 (2015).
- [54] S. Ikeda, K. Miura, H. Yamamoto, K. Mizunuma, H.D. Gan, M. Endo, S. Kanai, J. Hayakawa, F. Matsukura and H. Ohno, A perpendicular-anisotropy CoFeB-MgO magnetic tunnel junction, *Nature Materials* 9, 721-724 (2010).
- [55] R. Engel-Herbert and T. Hesjedal, Calculation of the magnetic stray field of a uniaxial magnetic domain, *Journal of Applied Physics* 97, 074504 (2005).
- [56] N. Kani, S.C. Chang, S. Dutta and A. Naeemi, A Model Study of an Error-Free Magnetization Reversal Through Dipolar Coupling in a Two-Magnet System, *IEEE Transactions on Magnetics* 52, 1-12 (2016).
- [57] A. Aharoni, Demagnetizing factors for rectangular ferromagnetic prisms, *Journal of Applied Physics* 83, 3432-3434 (1998).
- [58] K. Roy, S. Bandyopadhyay, J. Atulasimha, K. Munira and A.W. Ghosh, Energy dissipation and switching delay in spin-transfer torque switching of nanomagnets with low-saturation magnetization in the presence of thermal fluctuations, arxiv:1107.0387 (2011).
- [59] H. Keiji, N. Makoto, U. Tomomasa, A. Hisanori, I. Sumio, A. Yoshiaki, Y. Hiroaki and N. Akihiro, Effect of Self-Heating on Time-Dependent Dielectric Breakdown in Ultrathin MgO Magnetic Tunnel Junctions for Spin Torque Transfer Switching Magnetic Random Access Memory, *Japanese Journal of Applied Physics* 49, 04DD15 (2010).
- [60] C. Chul-Min, O. Young-Taek, K. Kyung-Jun, P. Jin-Suk, S. Hiroaki, M. Seiji, K. Sung-Kyu, L. Jeong-Yong and S. Yun-Heub, Temperature dependence of reliability characteristics for magnetic tunnel junctions with a thin MgO dielectric film, *Semiconductor Science and Technology* 31, 075004 (2016).
- [61] B. Oliver, G. Tuttle, Q. He, X. Tang and J. Nowak, Two breakdown mechanisms in ultrathin alumina barrier magnetic tunnel junctions, *Journal of Applied Physics* 95, 1315-1322 (2004).
- [62] C. Yoshida, M. Kurasawa, Y.M. Lee, K. Tsunoda, M. Aoki and Y. Sugiyama, A study of dielectric breakdown mechanism in CoFeB/MgO/CoFeB magnetic tunnel junction, in 2009 IEEE International Reliability Physics Symposium, pp. 139-142.
- [63] D.V. Dimitrov, Z. Gao, X. Wang, W. Jung, X. Lou and O.G. Heinonen, Dielectric breakdown of MgO magnetic tunnel junctions, *Applied Physics Letters* 94, 123110 (2009).
- [64] S. Amara-Dababi, R.C. Sousa, M. Chshiev, H. Béa, J. Alvarez-Hérault, L. Lombard, I.L. Prejbeanu, K. Mackay and B. Dieny, Charge trapping-detrapping mechanism of barrier breakdown in MgO magnetic tunnel junctions, *Applied Physics Letters* 99, 083501 (2011).
- [65] Y. Lu, M. Tran, H. Jaffrès, P. Seneor, C. Deranlot, F. Petroff, J.M. George, B. Lépine, S. Ababou and G. Jézéquel, Spin-Polarized Inelastic Tunneling through Insulating Barriers, *Physical Review Letters* 102, 176801 (2009).
- [66] Z. Kugler, V. Drewello, M. Schäfers, J. Schmalhorst, G. Reiss and A. Thomas, Temperature and bias voltage dependence of Co/Pd multilayer-based magnetic tunnel junctions with perpendicular magnetic anisotropy, *Journal of Magnetism and Magnetic Materials* 323, 198-201 (2011).
- [67] H. Kubota, A. Fukushima, K. Yakushiji, T. Nagahama, S. Yuasa, K. Ando, H. Maehara, Y. Nagamine, K. Tsunekawa, D.D. Djayaprawira, N. Watanabe and Y. Suzuki, Quantitative measurement of voltage dependence of spin-transfer torque in MgO-based magnetic tunnel junctions, *Nature Physics* 4, 37-41 (2008).
- [68] J.C. Sankey, Y.-T. Cui, J.Z. Sun, J.C. Slonczewski, R.A. Buhrman and D.C. Ralph, Measurement of the spin-transfer-torque vector in magnetic tunnel junctions, *Nature Physics* 4, 67-71 (2008).
- [69] M. Julliere, Tunneling between ferromagnetic films, *Physics Letters A* 54, 225-226 (1975).
- [70] J.C. Slonczewski, Currents, torques, and polarization factors in magnetic tunnel junctions, *Physical Review B* 71, 024411 (2005).
- [71] X. Waintal, E.B. Myers, P.W. Brouwer and D.C. Ralph, Role of spin-dependent interface scattering in generating current-induced torques in magnetic multilayers, *Physical Review B* 62, 12317-12327 (2000).
- [72] S. Hernández and R.H. Victora, Calculation of spin transfer torque in partially polarized spin valves including multiple reflections, *Applied Physics Letters* 97, 062506 (2010).
- [73] W. Zhu, Z. Zhang, J. Zhang and Y. Liu, Multiple Reflection Effect on Spin-Transfer Torque Dynamics in Spin Valves with a Single or Dual Polarizer, *SPIN* 05, 1550003 (2015).

- [74] J.Z. Sun and D.C. Ralph, Magnetoresistance and spin-transfer torque in magnetic tunnel junctions, *Journal of Magnetism and Magnetic Materials* 320, 1227-1237 (2008).
- [75] K. Bernert, Spin-transfer torques in MgO-based magnetic tunnel junctions, Doctoral Thesis, Technische Universität Dresden (2014).
- [76] S. Tyagi, M. Alavi, R. Bigwood, T. Bramblett, J. Brandenburg, W. Chen, B. Crew, M. Hussein, P. Jacob, C. Kenyon, C. Lo, B. McIntyre, Z. Ma, P. Moon, P. Nguyen, L. Rumaner, R. Schweinfurth, S. Sivakumar, M. Stettler, S. Thompson, B. Tufts, J. Xu, S. Yang and M. Bohr, A 130 nm generation logic technology featuring 70 nm transistors, dual Vt transistors and 6 layers of Cu interconnects, in *Proceedings of the International Electron Devices Meeting (IEDM) 2000*, pp. 567-570.
- [77] Z. Luo, A. Steegen, M. Eller, R. Mann, C. Baiocco, P. Nguyen, L. Kim, M. Hoinkis, V. Ku, V. Klee, F. Jamin, P. Wrschka, P. Shafer, W. Lin, S. Fang, A. Ajmera, W. Tan, D. Park, R. Mo, J. Lian, D. Vietzke, C. Coppock, A. Vayshenker, T. Hook, V. Chan, K. Kim, A. Cowley, S. Kim, E. Kaltalioglu, B. Zhang, S. Marokkey, Y. Lin, K. Lee, H. Zhu, M. Weybright, R. Rengarajan, J. Ku, T. Schiml, J. Sudijono, I. Yang and C. Wann, High performance and low power transistors integrated in 65nm bulk CMOS technology, in *Proceedings of the International Electron Devices Meeting (IEDM) 2004*, pp. 661-664.
- [78] S. Natarajan, M. Agostinelli, S. Akbar, M. Bost, A. Bowonder, V. Chikarmane, S. Chouksey, A. Dasgupta, K. Fischer, Q. Fu, T. Ghani, M. Giles, S. Govindaraju, R. Grover, W. Han, D. Hanken, E. Haralson, M. Haran, M. Heckscher, R. Heussner, P. Jain, R. James, R. Jhaveri, I. Jin, H. Kam, E. Karl, C. Kenyon, M. Liu, Y. Luo, R. Mehandru, S. Morarka, L. Neiberg, P. Packan, A. Paliwal, C. Parker, P. Patel, R. Patel, C. Pelto, L. Pipes, P. Plekhanov, M. Prince, S. Rajamani, J. Sandford, B. Sell, S. Sivakumar, P. Smith, B. Song, K. Tone, T. Troeger, J. Wiedemer, M. Yang and K. Zhang, A 14nm Logic Technology Featuring 2nd-Generation FinFET , Air-Gapped Interconnects, Self-Aligned Double Patterning and a 0.0588 m2 SRAM cell size, in *Proceedings of the International Electron Devices Meeting (IEDM) 2014*, pp. 3.7.1-3.7.3.
- [79] D. Houssameddine, U. Ebels, B. Delaet, B. Rodmacq, I. Firastrau, F. Ponthenier, M. Brunet, C. Thirion, J.P. Michel, L. Prejbeanu-Buda, M.C. Cyrille, O. Redon and B. Dieny, Spin-torque oscillator using a perpendicular polarizer and a planar free layer, *Nature Materials* 6, 447-453 (2007).
- [80] O. Boulle, V. Cros, J. Grollier, L.G. Pereira, C. Deranlot, F. Petroff, G. Faini, J. Barnas and A. Fert, Shaped angular dependence of the spin-transfer torque and microwave generation without magnetic field, *Nature Physics* 3, 492-497 (2007).
- [81] J.-V. Kim, Q. Mistral, C. Chappert, V.S. Tiberkevich and A.N. Slavin, Line Shape Distortion in a Nonlinear Auto-Oscillator Near Generation Threshold: Application to Spin-Torque Nano-Oscillators, *Physical Review Letters* 100, 167201 (2008).
- [82] W.F. Brown, Thermal Fluctuations of a Single-Domain Particle, *Physical Review* 130, 1677-1686 (1963).
- [83] T. Chen, Wideband amplifier design for STO technology, Master's thesis, KTH Royal Institute of Technology (2011).
- [84] X. Meng, L. Zhou, F. Lin and C.H. Heng, 390–640MHz tunable oscillator based on phase interpolation with –120dBc/Hz in-band noise, in *2015 IEEE Custom Integrated Circuits Conference (CICC)*, pp.
- [85] A.S. Sedra and K.C. Smith, *Microelectronic Circuits*, Oxford University Press, New York (2004).

Figures

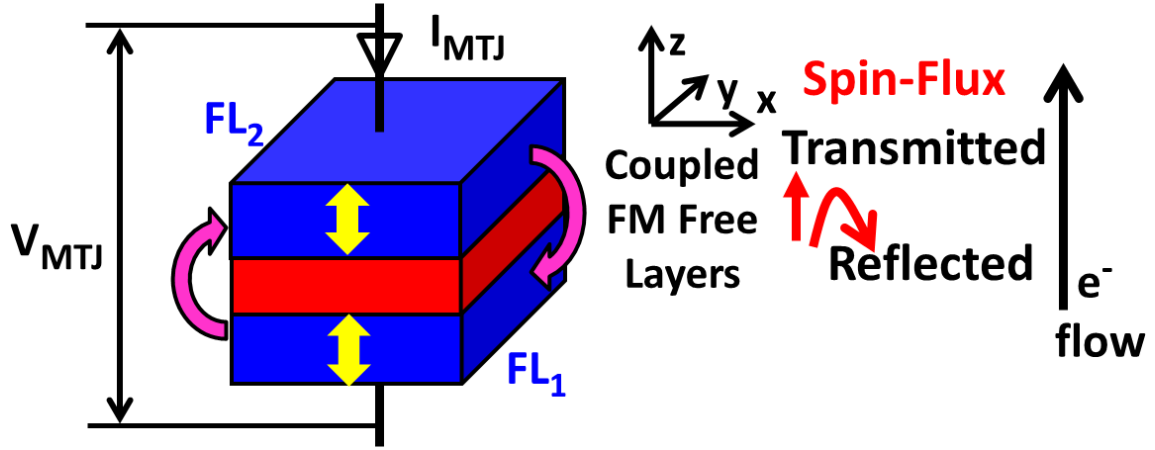


Figure 1. Conceptual illustration of a pMTJ with a dipolar coupled dual free-layer, without any pinned layer. It is driven by a uni-directional current from FL₂ to FL₁. The transmitted spin-flux with a vector parallel to the magnetization of FL₁ acts on FL₂, while reflected spin-flux with a vector anti-parallel to the magnetization of FL₂ acts on FL₁, which for a set of electronic and geometric constraints results in a self-sustained switching of both the free layers producing AC oscillations for a DC bias. When this pMTJ is driven via tunable DC current source I_{MTJ} , the device is in a CCO configuration.

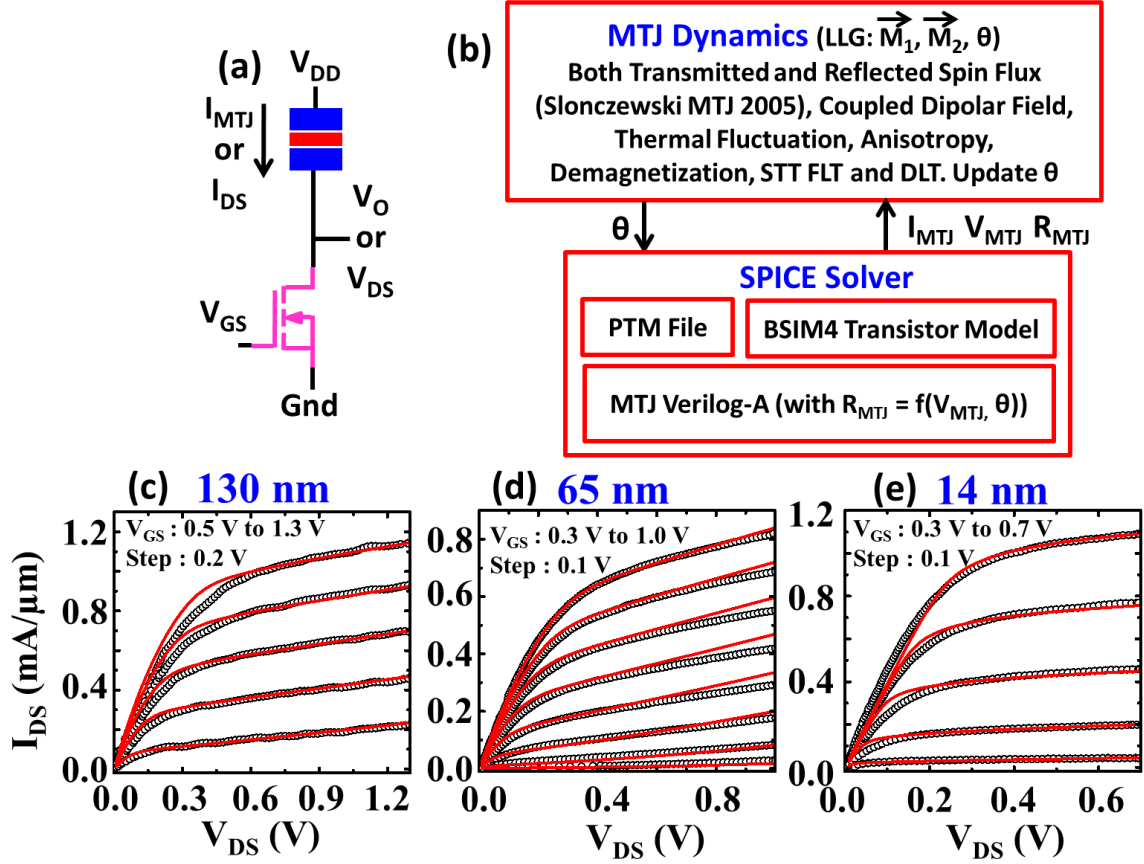


Figure 2. (a) VCO configuration with a pMTJ driven via tunable DC V_{GS} for a fixed V_{DD} (gate-control) or tunable DC V_{DD} for a fixed V_{GS} (drain-control). (b) Schematic summary of the simulation framework expounded in the methodology section. (c-e) Published experimental data (black circles) of the NMOS output characteristics fitted (red line) against the BSIM4 model used in a spice solver for three representative CMOS nodes. For (c) 130 nm node fitting against Fig. 4 of Ref. [76] from Intel, (d) 65 nm node fitting against Fig. 6 of Ref. [77] from IBM, Chartered and Infineon, and (e) 14 nm node fitting against Fig. 5 of Ref. [78] from Intel.

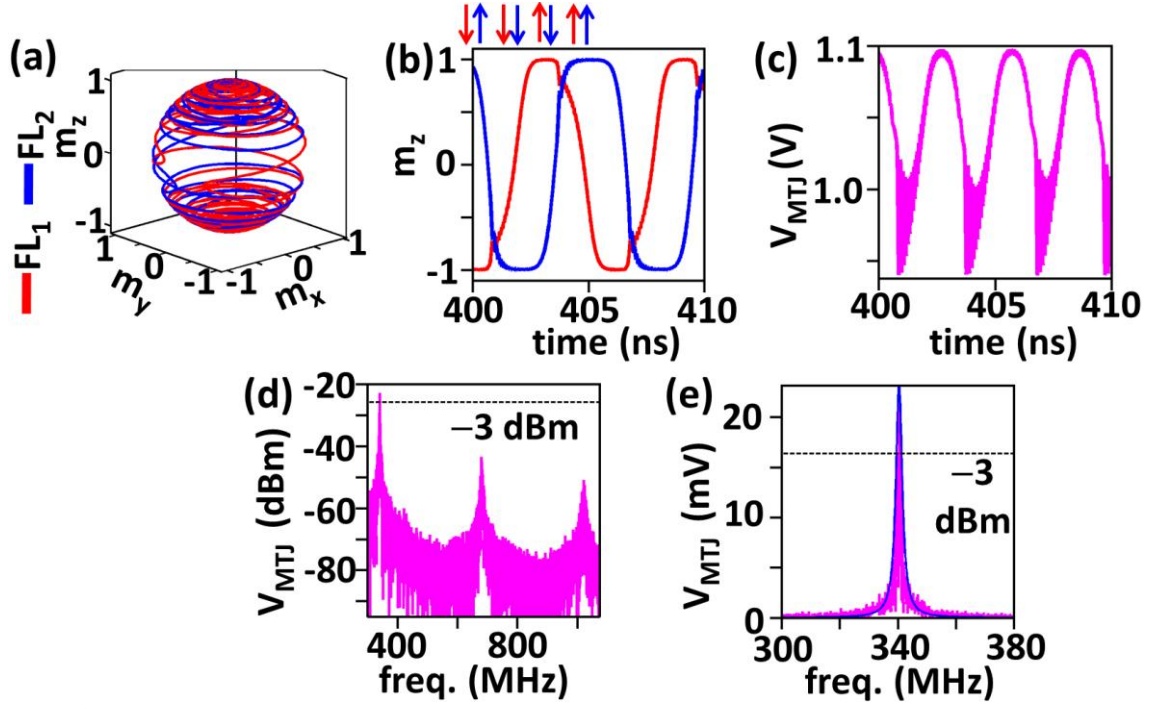


Figure 3. Operation principle (without a thermal field) of the device driven by a constant current. (a) 400-405 ns dynamics of the magnetization unit vector $\mathbf{m} = [m_x, m_y, m_z]^T$. (b) Full-switching of both m_z . (c) Output voltage oscillations V_{MTJ} . FFT of V_{MTJ} in dBm (d) and mV (e) demonstrating a fundamental tone along with the first two harmonics (in (d)) and the Lorentzian fit (blue line in (e)). The dashed black lines are -3dBm line which cuts through half-power points. Lorentzian fit is used to extract the linewidth and the quality factor of the oscillator.

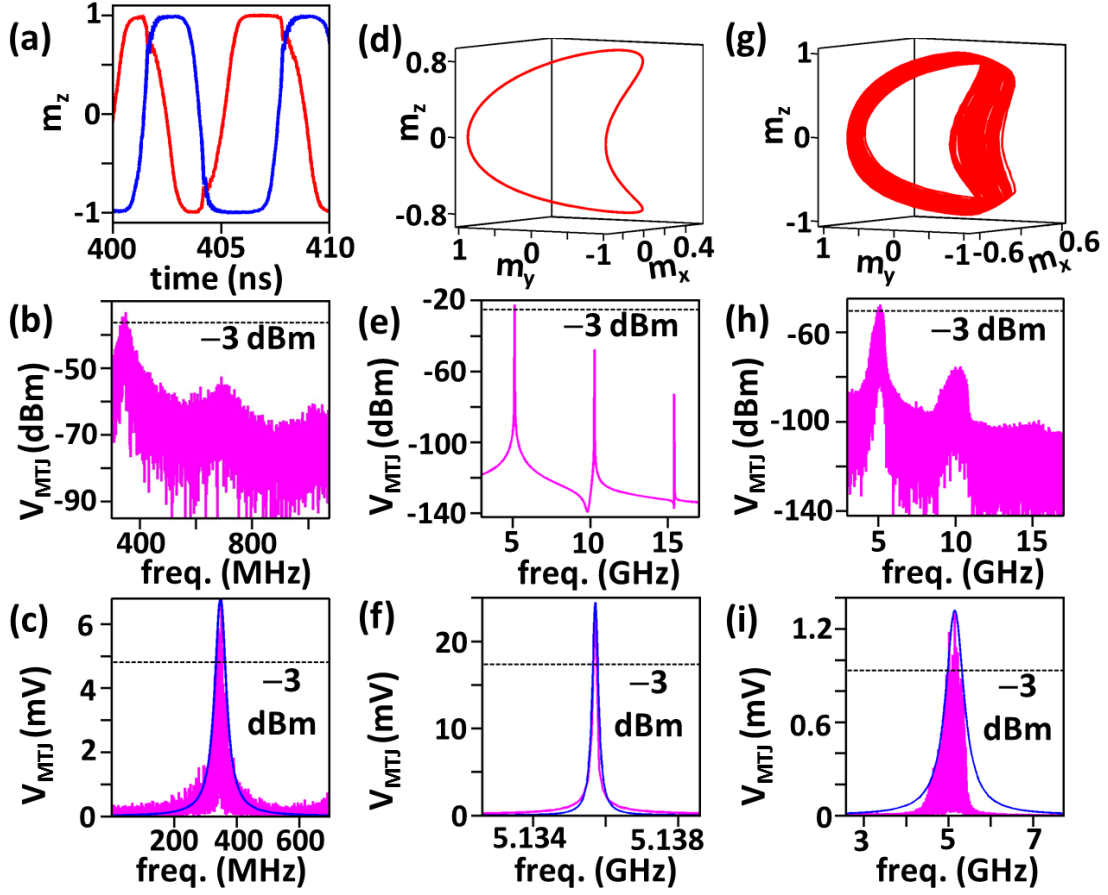


Figure 4. Effect of the thermal fluctuation field (300 K) on the proposed oscillator (a-c) is contrasted with an orthogonal STNO (c-i) of 60nm×40nm×5nm(1.8nm) with an in-plane fixed layer (in place of FL₁) and a perpendicular free layer (in place of FL₂) operating at 5.1 GHz with 70 μ A fixed current without an external bias field. (c-f) STNO without a thermal field clearly shows the precessional orbit (d) and FFT of the voltage across the MTJ (e, f). (g-i) STNO with a thermal field shows randomness introduced in the orbit ((d, g) illustration represents 400-450 ns of precession), and the linewidth broadening in FFT in (h, i). In FFT plots, the dashed black lines are -3dBm line which cuts through half-power points and thus determines the linewidth and the quality factor of the oscillator, while the blue lines are the Lorentzian fit via which the linewidth and the quality factor of the oscillator are extracted.

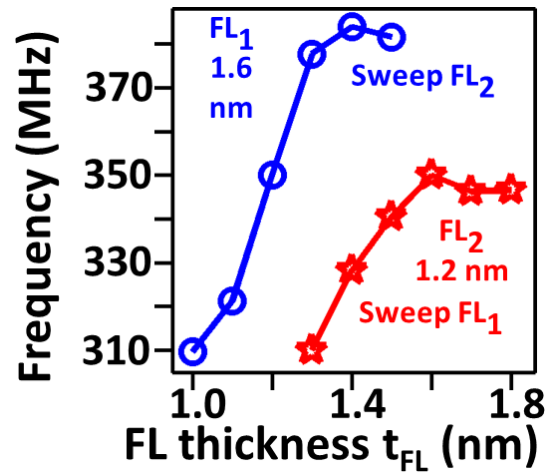


Figure 5. Effect of the FL thickness on the oscillation frequency for a representative I_0 of 500 μA . MTJ can thus be designed to meet the frequency specifications of an oscillator over a wide frequency range.

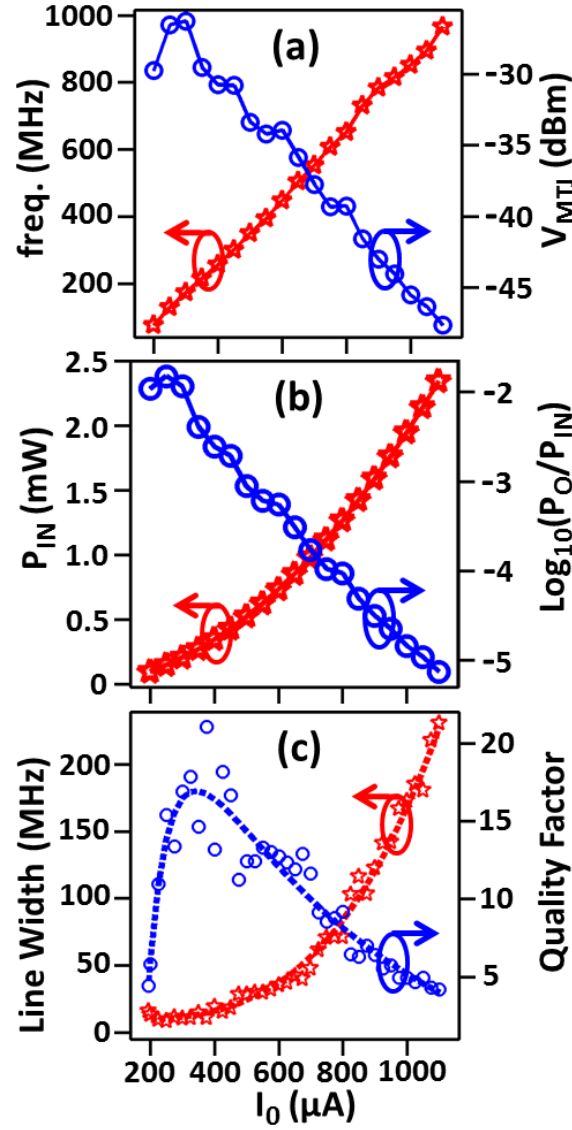


Figure 6. Effect of a constant current I_0 on (a) the frequency and the output voltage oscillations, (b) the input power consumed P_{IN} and the power efficiency (P_O/P_{IN}) i.e. the delivered output power to the consumed power, (c) the linewidth and the quality factor (Q) of the oscillator. Dashed lines are the fit to the data to exhibit an overall trend. (b) Consumed power decreases directly with the current thereby improving the power efficiency especially at the lower frequencies. (c) Linewidth (frequency spectra) narrows at the smaller currents (frequencies) which improve the quality factor ($=$ Center Frequency / Linewidth) at intermediate frequencies up to 21.

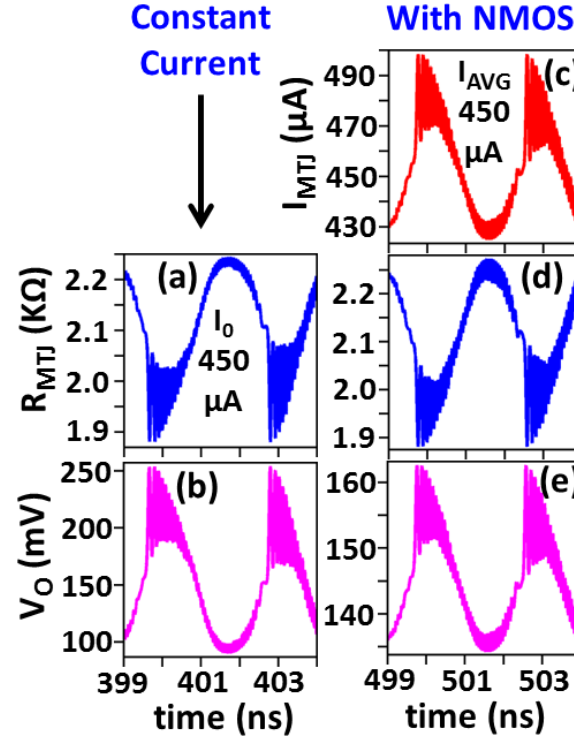


Figure 7. Effect of replacing (a, b) a constant current source with (c-e) an NMOS (W/L=28) to drive the MTJ. For (b) $V_O = 1.1 - V_{MTJ}$ for an appropriate comparison with (e). For an NMOS, the drain current also oscillates in anti-phase with the resistance, thereby reducing the output swing which is approximately given by eq. (10). I_0 is chosen equal to the average drain current, and the complementary MTJ voltage is used as V_O for a constant current case, for the rightful comparison.

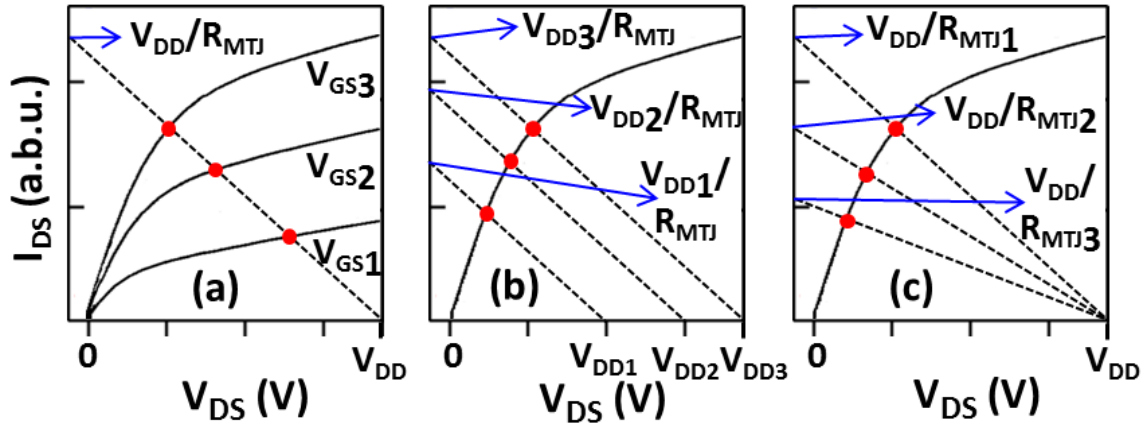


Figure 8. Conceptual illustration of load-line analysis to show the effect of sweeping (a) V_{GS} , (b) V_{DD} and (c) MTJ cross-section. Larger index in the subscript represents a larger magnitude of the corresponding quantity. Solid black line is the NMOS output characteristics. Dashed black line is the R_{MTJ} output characteristic, where R_{MTJ} is treated as a constant trivial resistor in this illustration. Quiescent point is marked via red dot at the point of an intersection of the R_{MTJ} and the NMOS characteristics. This serves as a visual aid for understanding the data for the effect of the respective parameters shown in the subsequent figures.

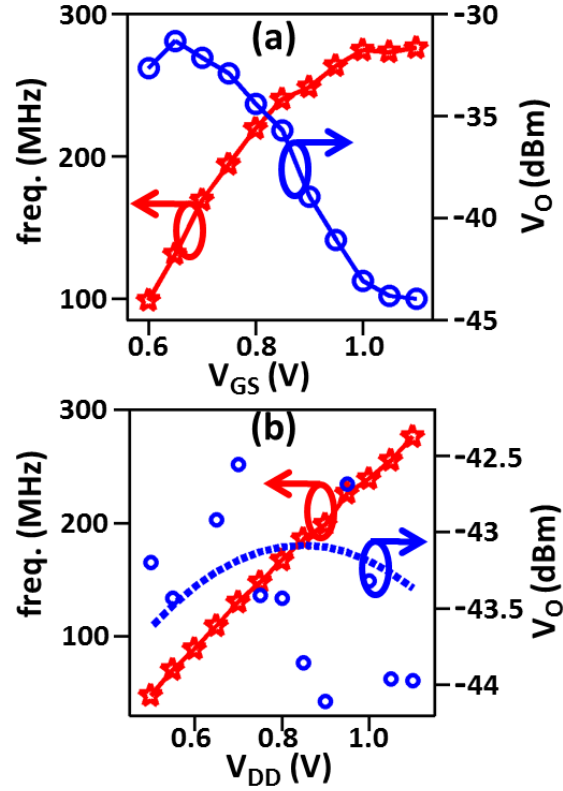


Figure 9. Effect of sweeping (a) gate voltage V_{GS} and (b) node voltage V_{DD} on frequency and output voltage V_O . Dashed lines in (b) is the fit to the data to exhibit an overall trend for V_O .

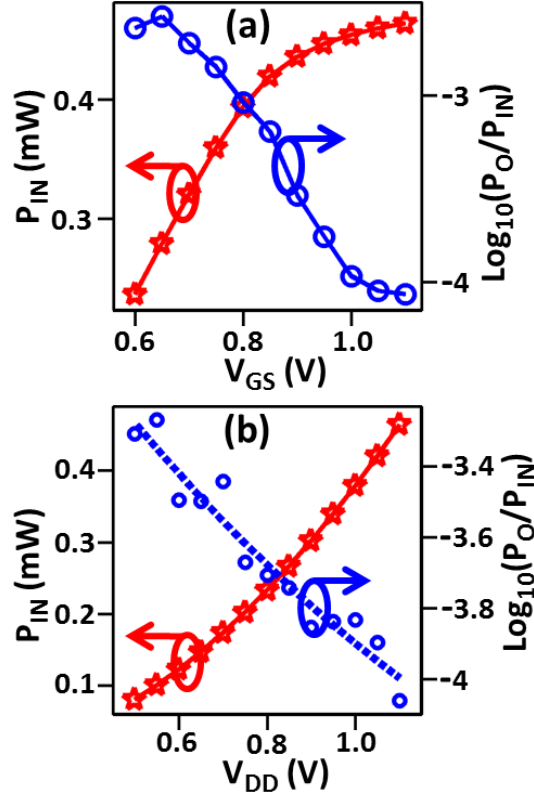


Figure 10. Effect of sweeping (a) gate voltage V_{GS} and (b) node voltage V_{DD} on consumed input power P_{IN} and power efficiency P_O/P_{IN} . Dashed line in (b) is the fit to the data to exhibit an overall trend for P_O/P_{IN} .

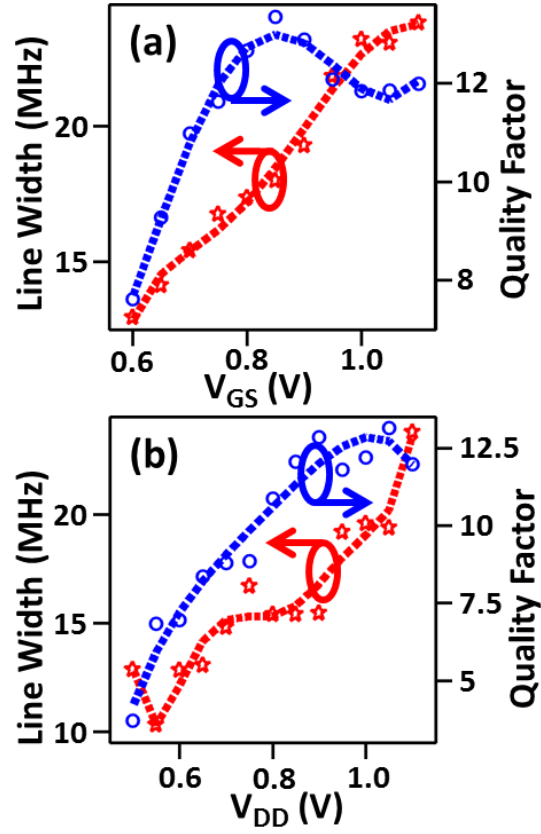


Figure 11. Effect of sweeping (a) gate voltage V_{GS} and (b) node voltage V_{DD} on Linewidth and quality factor Q . Dashed lines in are the fit to the data to exhibit an overall trend.

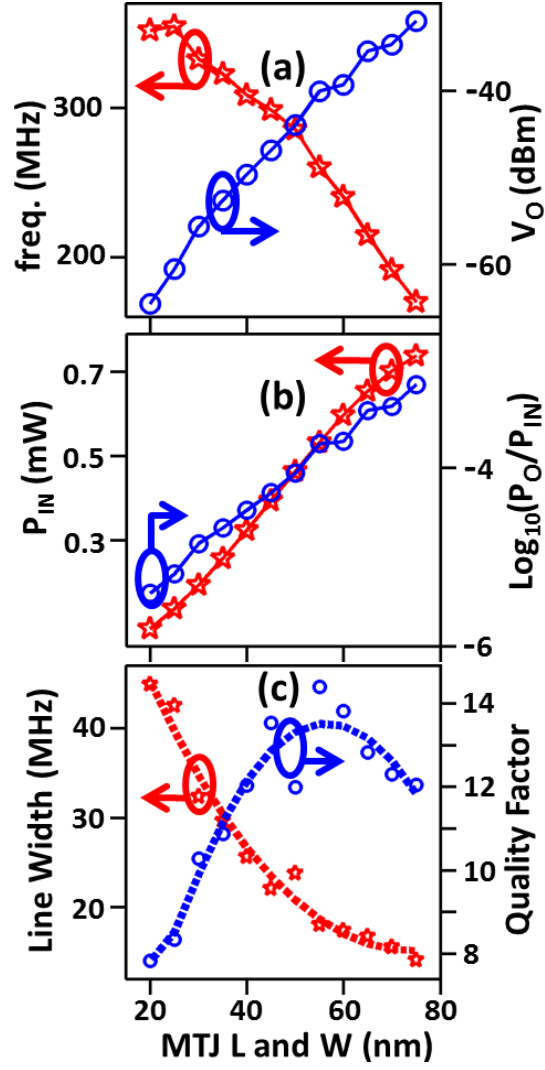


Figure 12. Effect of sweeping MTJ cross-section (length=width) on (a) frequency and output voltage V_O , (b) input power P_{IN} and power efficiency P_O/P_{IN} , and (c) Linewidth and quality factor Q . Dashed lines in (c) are the fit to the data to exhibit an overall trend.

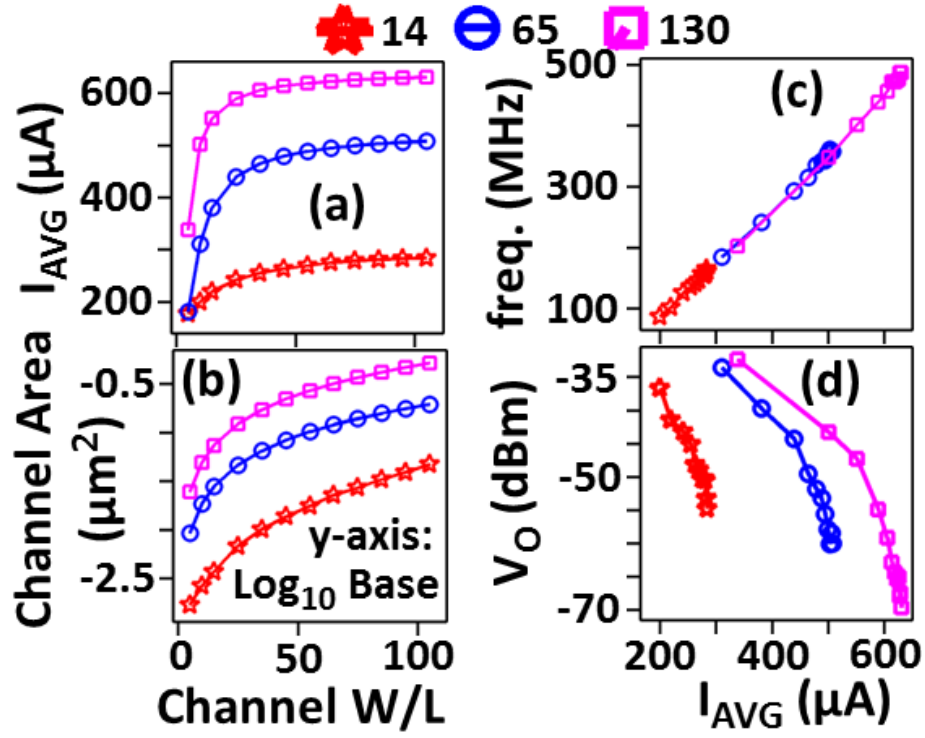


Figure 13. Effect of W/L of transistors on performance across 14 nm, 65 nm and 130 nm node operating at the full scale node voltage (0.7, 1.1, 1.3 V) i.e. $V_{DD}=V_{GS}$. (a) Average operating current for the oscillator. (b) Channel area for the reference. Output frequency (c) and the signal amplitude (d).

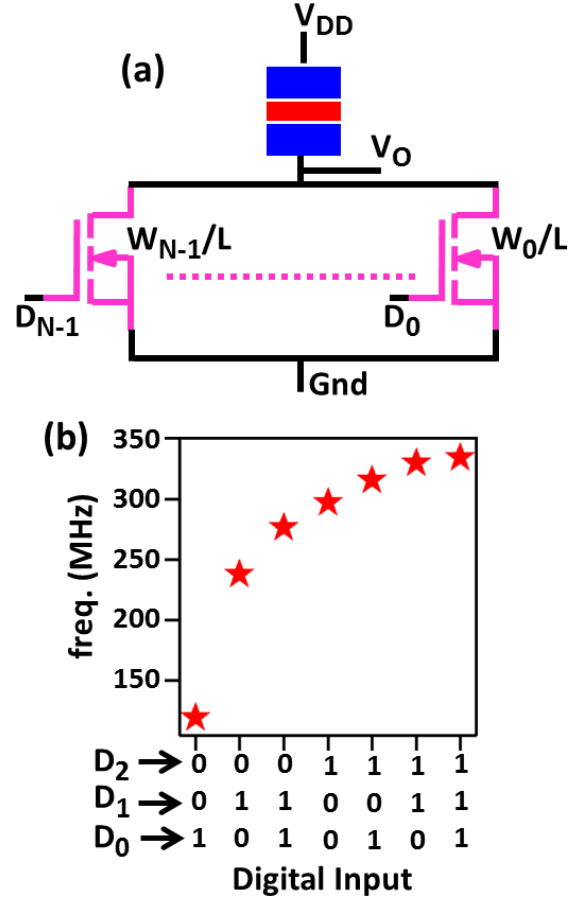


Figure 14. (a) Re-designing a VCO into a DCO configuration by splitting the effective transistor width across wire-ORed N -transistors, driven by an N -bit digital control D_0 to D_{N-1} . Effective width for a bulk-NMOS or number of fins for a FinFET of transistor ' m ', driven by a bit D_m , is twice the width or number of fins of a transistor ' $m-1$ ' where $m \in [1, N-1]$. (b) Frequency obtained for a 3-bit DCO with channel widths of $W_2 = 2$ $W_1 = 4$ $W_0 = 28$ L , with a tuning ratio of 2.8.

Table I. Summary of a comparison with other designs in the literature.

Criteria	pp 9 (C)	pp 9, β (NMOS)	STNO κ , χ , δ (pi/ip) (C)	Ring λ , ζ [42]
Freq. (f) (MHz)	71 – 965	47.6 – 276.3	600 – 4000 [20, 41, 79, 80]	480-1100
f_{\max}/f_{\min}	13.6	5.8	~ 2 &	1.25
V_O (dBm)	–26 to –48	–31 to –44	–42 &	–2.97
P_O/P_{IN} (%)	1.5 to 0.0007	0.26 to 0.008	0.12 &	13.1
Q	4.2 - 21	3.7 – 13.3	8-39 &	–120 to –108 dBc/Hz Φ
Area (μm^2)	0.0025 *	0.0388 #	0.0105 *&	14784 Ψ

C: Driven by Current Source; * MTJ area; # Channel Area; Ψ Core Area;

9. $50 \times 50 \times 1.6(1.2)$; β . Gate Control 65 Node $W/L=21$; δ . $50 \times 40 \times t_1(t_2)$; κ . ii and pp need an external B-Field to precesses. χ . TMR based without any additional locking or post-processing circuit; δ See Table 1 of Ref. [41]; & Best of the results of Ref. [41]; λ LC is not compared, because in the sub-GHz range the size of an on-chip inductor and a capacitor is in hundreds of μm^2 . Its comparison is better suited in high GHz range. Φ Phase Noise (not Q); ζ with PLL lock (not for free-running case).